

A Comparison between the Only Two Documented Tornado Outbreak Events in China: Tropical Cyclone versus Extratropical Cyclone Environments

JINGYI WEN,^a ZHIYONG MENG,^a LANQIANG BAI,^b AND RUILIN ZHOU^{c,d}

^a *Department of Atmospheric and Oceanic Sciences, School of Physics, and China Meteorological Administration Tornado Key Laboratory, Peking University, Beijing, China*

^b *China Meteorological Administration Tornado Key Laboratory and Foshan Tornado Research Center, CMA, and Southern Marine Science and Engineering Guangdong Laboratory (Zhuhai), Guangdong, China*

^c *Chongqing Research Institute of Big Data, Peking University, Chongqing, China*

^d *Key Laboratory of Urban Meteorology, China Meteorological Administration, Beijing, China*

(Manuscript received 10 May 2023, in final form 18 January 2024, accepted 12 February 2024)

ABSTRACT: This study documents the features of tornadoes, their parent storms, and the environments of the only two documented tornado outbreak events in China. The two events were associated with Tropical Cyclone (TC) Yagi on 12 August 2018 with 11 tornadoes and with an extratropical cyclone (EC) on 11 July 2021 (EC 711) with 13 tornadoes. Most tornadoes in TC Yagi were spawned from discrete minisupercells, while a majority of tornadoes in EC 711 were produced from supercells imbedded in QLCs or cloud clusters. In both events, the high-tornado-density area was better collocated with the K index rather than MLCAPE, and with entraining rather than non-entraining parameters possibly due to their sensitivity to midlevel moisture. EC 711 had a larger displacement between maximum entraining CAPE and vertical wind shear than TC Yagi, with the maximum entraining CAPE better collocated with the high-tornado-density area than vertical wind shear. Relative to TC Yagi, EC 711 had stronger entraining CAPE, 0–1-km storm relative helicity, 0–6-km vertical wind shear, and composite parameters such as an entraining significant tornado parameter, which caused its generally stronger tornado vortex signatures (TVSs) and mesocyclones with a larger diameter and longer life span. No significant differences were found in the composite parameter of these two events from U.S. statistics. Although obvious dry air intrusions were observed in both events, no apparent impact was observed on the potential of tornado outbreak in EC 711. In TC Yagi, however, the dry air intrusion may have helped tornado outbreak due to cloudiness erosion and thus the increase in surface temperature and low-level lapse rate.

KEYWORDS: Entrainment; Dry intrusions; Extratropical cyclones; Extreme events; Tornadoes; Tropical cyclones

1. Introduction

A tornado outbreak event is defined as 10 or more tornadoes from a single, organized weather system (Galway 1977). Tornado outbreaks often occur in the United States (Zhou et al. 2022). Even using a relatively high criterion to determine tornado outbreak events in which 10 or more tornadoes of at least level EF1 must occur within 6 h, Anderson-Frey et al. (2018) showed that 134 tornado outbreaks occurred in the contiguous United States from 2003 to 2015, producing 5343 tornadoes; approximately 10 outbreaks produced 411 tornadoes on average per year.

Tornado outbreaks are often associated with tropical cyclones (TCs) and extratropical cyclones (ECs) (Gentry 1983; McCaul 1993; Newton 1967; Hamill et al. 2005). For example, TC Ivan produced 118 tornadoes from 15 to 18 September 2004 (Baker et al. 2009), and an EC produced 361 tornadoes from 3 to 11 May 2003 in the United States (Hamill et al. 2005). Studies on tornado outbreaks in the United States have identified some synoptic features that are favorable for tornado outbreaks, such as relatively strong upper-level troughs and low-level thermal advection (Mercer et al. 2012). Strong vertical wind shear and storm relative helicity (SRH) have

been identified as the most distinguishable dynamic parameters for tornado outbreak events (Shafer et al. 2009; Mercer et al. 2012).

Tropical cyclones are one major environment conducive to tornado outbreaks, and the northeast quadrant (Edwards et al. 2012; Bai et al. 2020b) or downshear-right quadrant (Schenkel et al. 2021) is typically the highest-frequency region. Landfalling TCs tend to produce tornadoes mainly due to strong near-surface vertical wind shear (Novlan and Gray 1974) and SRH (McCaul 1991). Tornado outbreaks in TC environments have been attributed mainly to two aspects. One is the midlatitude environmental wind shear. TC tornado outbreaks are often accompanied by an enhanced upper-level (200 hPa) jet streak to the north (Cohen 2010) or associated with a midlatitude trough (Verbout et al. 2007). Studies have shown that TCs produce more tornadoes when they begin to recurve, interact with or become embedded within midlatitude westerlies (Verbout et al. 2007; Moore and Dixon 2011, 2015). Interactions with midlatitude westerlies may intensify the across-TC shear, and this change may enhance the localized shear and helicity and thus cause tornado outbreaks. Bai (2021) revealed that the interactions among the typhoon circulation, subtropical high and midlevel trough may cause the strongest in–up–out radial wind variation and thus contribute to relatively large helicity in the northeast quadrant of TC outbreak events in China.

Corresponding author: Zhiyong Meng, zymeng@pku.edu.cn

DOI: 10.1175/WAF-D-23-0083.1

© 2024 American Meteorological Society. This published article is licensed under the terms of the default AMS reuse license. For information regarding reuse of this content and general copyright information, consult the AMS Copyright Policy (www.ametsoc.org/PUBSReuseLicenses).

Brought to you by Pennsylvania State University, Paterson Library | Unauthenticated | Downloaded 03/23/24 05:07 PM UTC

The other aspect is midlevel dry air intrusion which has been regarded favorable for tornado outbreaks in TC environment (Curtis 2004; Cohen 2010). The impact of midlevel dry air intrusion on TC tornado outbreaks remains uncertain. One hypothesis is that midlevel dry air causes the increase in convective instability due to an increased environment lapse rate (McCaul 1987). Dry air may also enhance evaporative cooling of ambient stratus clouds around the convection at middle levels and thus increase the lapse rate and convective available potential energy (CAPE). In addition, dry air may erode middle and upper-level cloudiness and allow full insolation to penetrate to near the surface and thus increase surface-based CAPE (Curtis 2004). In the meantime, at the edge of the cloudiness, surface baroclinic zones may be produced, which may help to enhance low-level vertical shear.

Although Curtis (2004) demonstrated that 11 out of 13 tornado outbreak events in the United States were associated with middle or low-level dry air intrusion, he admitted that it is possible that the reasons could be the more uniformly moist lowest layer, and midlevel dry intrusions did not produce a consistent pattern with respect to temperature lapse rates. Similar notes were also made in Rasmussen and Blanchard (1998) and Thompson et al. (2003). Another reason for the mixed impact of dry air on tornado outbreaks could be the lack of quantitative and consistent definition of dry air in the literature. Raveh-Rubin (2017) defined dry air intrusions as dry, deeply descending airstreams from the upper troposphere toward the planetary boundary layer (PBL). McCaul (1987) classified dry air into two types. One is pockets of dry low-level air that may be associated with subsidence. The other is mid and upper-level dry intrusion fed by a larger-scale reservoir of dry air. In most published papers that mentioned the possible impact of dry air intrusion on tornado outbreaks, the evidence of dry air intrusion was mostly demonstrated using a single radiosonde with increased dewpoint depression, which may not be able to represent spatial and temporal variations in the approximate environment of tornado outbreak events. Consequently, whether the existence of dry air intrusion is just an association with or a cause for tornado outbreaks have not been clearly shown in the literature.

CAPE has been shown to be poorly correlated with tornado locations in TC environments (McCaul 1991). CAPE in a TC environment is generally small. By including the effects of entrainment of environmental air, Molinari et al. (2012) proposed entraining CAPE (E-CAPE) to adequately represent the asymmetric distribution of convection around TCs. Sueki and Niino (2016) demonstrated a good collocation between TC tornadoes and large E-CAPE and SRH values in the northeast quadrant of a TC, with larger values found in tornadic TCs than in nontornadic TCs. Similar features were also reported for TC tornadoes in China (Bai et al. 2020b).

Relative to TCs, ECs are another primary synoptic feature producing tornado outbreaks, with their warm sector being the most favorable region (e.g., Johns and Doswell 1992). In typical ECs that cause tornado outbreaks, an upper-level jet at ~ 500 hPa is located near the center of the EC, and this jet strengthens vertical shear and advects cool, dry air into the upper and middle troposphere, while low-level southerly

winds advect warm and moist air into the warm sector, producing a region of convective instability. Based on a composite analysis of EC tornado outbreaks in the United States, Tochimoto and Niino (2016) found that ECs with tornado outbreaks have larger magnitudes of SRH and CAPE with a larger areal extent for certain high values than ECs without tornado outbreaks. The larger CAPE values are due to larger amounts of low-level water vapor, while greater SRH values are due to the stronger low-level southerly wind. Similar to the TC environment, the E-CAPE, entraining energy helicity index (E-EHI), and entraining significant tornado parameter (E-STP) values are more optimally collocated with tornado locations in the EC environment than their non-entraining counterparts (Tochimoto et al. 2019).

The above review shows different environments that are favorable for tornado outbreaks. It is interesting to know the differences between these environments. There have been comparative studies between ECs with and without tornado outbreaks (Tochimoto and Niino 2016; Tochimoto et al. 2019) in the literature. Differences in environmental parameters of TC tornadoes from non-TC tornadoes were also examined in Edwards et al. (2012) which showed that TC tornado environment has much greater deep-tropospheric moisture, the associated reduced lapse rates, lower CAPE, and smaller and more compressed distributions of parameters derived from CAPE and vertical shear. Sueki and Niino (2016) examined the differences between tornadic and nontornadic TCs. However, there has been no direct comparison of tornado outbreaks between TC and EC. This study is to compare the environments of two tornado outbreak events that occurred in a tropical cyclone and an extratropical cyclone in China, which are also the only two tornado outbreak events that have been documented in China to date.

Unlike the United States, tornado outbreaks rarely occur in China. The lower low-level vertical wind shear in the tornado season of the most high-tornado-frequency area in China leads to a relatively low likelihood of multiple tornadoes occurring in a short period and thus a much lower possibility of tornado outbreaks (Zhou et al. 2022). The only two documented tornado outbreak events that occurred in China were associated with TC Yagi in August 2018, producing 11 tornadoes, and an EC in July 2021, producing 13 tornadoes. Interestingly, these two events both occurred in summer and produced tornadoes mainly in the same area. Some studies have revealed that the environment of TC Yagi was favorable for tornadogenesis, including significant dry air intrusions and the interaction of Yagi with an approaching midlatitude, midlevel trough (Bai et al. 2020b); these conditions caused the overlap of high SRH and E-CAPE values in the northeast quadrant of TC Yagi (Bai 2021). Unfortunately, how the dry air intrusion affected the tornadogenesis was not examined quantitatively. Interestingly, an apparent dry air intrusion was also observed in the EC tornado outbreak events. However, the environment of this EC tornado outbreak event has not been examined in the literature.

The purpose of this paper is to document the characteristics of the only two observed tornado outbreak events in China and their differences in tornado distribution, parent storm

modes, and environmental features. Their differences in environmental features from tornado outbreaks in the United States will be examined as well. This work is unique in four aspects. First, this documents the only two known tornado outbreaks in China to date; second, this is the first direct comparison of tornado outbreak events that occurred in nearly the same location, but one in a TC environment and the other in an EC environment, with apparent differences observed in their parent storms and associated thermodynamic and dynamic environmental parameters; Third, features of these two tornado outbreak events in China were compared with statistics of tornado outbreak events in the United States. Last but not the least, detailed analyses were performed on the impact of dry air on tornadogenesis, which provided new insight on the scale of dry air impact on tornadogenesis potential using hourly ERA5 analyses at tornado locations, relative to previous speculations obtained using radiosondes with coarse temporal and spatial resolutions.

Section 2 presents a summary of the data and analysis methods. Section 3 provides an overview of the two tornado outbreak cases. The characteristics of tornadoes and their parent storms in both events are compared in section 4. Section 5 examines the distinctions in the environment between the two events and their differences from those in the United States. In particular, a detailed analysis on the impact of dry air is performed. Section 6 gives a summary.

2. Data and method

a. Detection of TC and EC centers

The TC best-track data were obtained from the China Meteorological Administration (Ying et al. 2014; Lu et al. 2021; <https://tcddata.typhoon.org.cn>). The fifth generation European Centre for Medium-Range Weather Forecasts (ECMWF) reanalysis dataset (ERA5, available online at <https://cds.climate.copernicus.eu/cdsapp#!/dataset/reanalysis-era5-single-levels?tab=overview>) with a 1-h interval and $0.25^\circ \times 0.25^\circ$ horizontal resolution was used to determine the central location of EC and to analyze the synoptic environmental features. To compare the locations of tornadoes with respect to cyclone centers, we defined the EC center using a method similar to that applied for TCs. Because the TC center was determined mostly using the minimum sea level pressure (MSLP) and because the central location of the TC after the extratropical transition (ET) process is usually determined using 850-hPa charts, the central location of the EC was defined by the lowest geopotential height at 850 hPa.

b. Detection of tornado, mesocyclone, and TVS

Records of tornadoes were obtained from local meteorological agencies, social media and published papers. The rotational velocity and life-span data of mesocyclones and TVS were determined manually using Gibson-Ridge Analyst version 2 (GR2Analyst 2.0) radar-viewing software. S-band radars with 9 elevation angles of 0.5° , 1.4° , 2.4° , 3.3° , 4.3° , 6.0° , 9.9° , 14.6° , and 19.5° were used to identify mesocyclones and TVSS. The time needed for completing one volume scan is 6 min. The azimuthal and radial resolutions are, respectively,

1° and 1 km for reflectivity and 1° and 250 m for radial velocity. The data range is 460 km for reflectivity and 230 km for radial velocity.

We defined a mesocyclone following Bai et al. (2022) as follows: 1) the maximum reflectivity is equal to or larger than 40 dBZ; 2) the difference between the maximum positive radial velocity and the maximum negative radial velocity exceeds 20 m s^{-1} ; 3) the distance between the maximum positive radial velocity and the maximum negative radial velocity is less than 10 km and larger than 1.5 km; 4) cyclonic shear exists; and 5) more than one scan and one elevation angle satisfy the above criteria (McCaul et al. 2004). Additionally, we defined TVS following Meng and Yao (2014): two pixels next to each other or spaced at most at a distance of one pixel, near a mesocyclone, with cyclonic shear, and with a radial velocity difference no less than 20 m s^{-1} .

The intensity of a mesocyclone is measured using rotational velocity, which was calculated as half of the difference between the maximum positive radial velocity and the minimum negative radial velocity across the mesocyclone center at 0.5° elevation. The diameter of a mesocyclone was estimated as the distance between the maximum positive radial velocity and the maximum negative radial velocity across the mesocyclone center at 0.5° elevation. TVS intensity was calculated as radial velocity difference between two pixels next to each other or spaced at most at a distance of one pixel near the location of the tornado at 0.5° elevation.

Six radars were used for the TC Yagi event including Binzhou, Weifang, Xuzhou, Huaian, Nanjing, and Tanggu, and five radars were used for the EC 711 event including Puyang, Jianan, Binzhou, Cangzhou, and Qiqihaer. The mesocyclones had a range and beam height of 25–120 km from the radar site and 260 m–9.6 km above the ground, respectively, at tornado generating times.

c. Environmental parameters

The environmental parameters were calculated using the ERA5 dataset. CAPE is the amount of buoyant energy available to accelerate a parcel vertically and is calculated by integrating the buoyancy of a lifted parcel between the level of free convection (LFC) and the equilibrium level (EL) as follows:

$$\text{CAPE} = \int_{\text{LFC}}^{\text{EL}} \frac{T'_v - T_v}{T_v} g dz, \quad (1)$$

where T'_v is the virtual temperature of the lifted parcel, T_v is the ambient virtual temperature and g is the gravitational acceleration. MLCAPE was calculated using a parcel lifted from a mixed layer in the lowest 100 hPa. We calculated E-CAPE by updating T'_v considering the effect of entrainment using the algorithm of Sueki and Niino (2016), which is based on the Lagrangian parcel model (Romps and Kuang 2010). The ascending air parcel was assumed to entrain environmental air at a constant mass entrainment rate (λ). Bai et al. (2020b) suggested that a mass entrainment rate of $40\% \text{ km}^{-1}$ works best for TC tornadoes in China. Consequently, in the

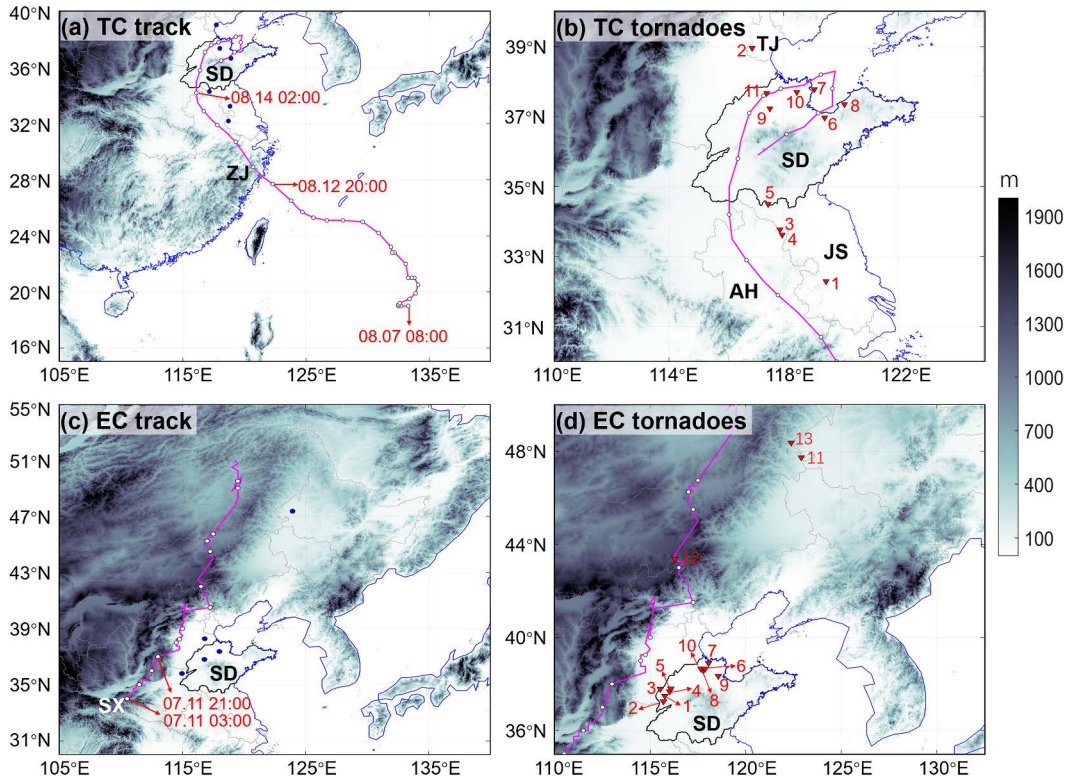


FIG. 1. Track of (a) TC Yagi and (c) EC 711 with the white dots denoting the TC or EC centers every 6 h and the black dots denoting radar locations used to analyze the parent storms of corresponding tornadoes. The distribution of tornadoes associated with (b) TC Yagi and (d) EC 711 are given in red triangles with the numbers of the tornadoes labeled as listed in Tables 1 and 3, respectively. Terrain heights (shaded; m) are shown for reference. “ZJ,” “SX,” “AH,” “JS,” “SD,” and “TJ” denote Zhejiang, Shaanxi, Anhui, Jiangsu, Shandong Provinces, and Tianjin metropolitan city, respectively. The boundary of Shandong Province is highlighted in black. The coastline is plotted in blue.

present study, E-CAPE was calculated with the λ value of $40\% \text{ km}^{-1}$.

The K index is a measure of the potential for a thunderstorm to develop, calculated from the temperature and dewpoint temperature in the lower part of the atmosphere:

$$K = (T_{850} - T_{500}) + T_{d850} - (T_{700} - T_{d700}), \quad (2)$$

where T is the temperature, and T_d is the dewpoint temperature. The numbers denote pressure levels.

The SRH gives the potential for rotational characteristics of convective storms (Davies-Jones et al. 1990). The SRH was calculated by integrating the storm-relative streamwise vorticity from the ground to a given altitude (Davies-Jones 1984):

$$\text{SRH} = \int_0^H (\mathbf{V}_h - \mathbf{C}) \cdot \left(\mathbf{k} \times \frac{\partial \mathbf{V}_h}{\partial z} \right) dz, \quad (3)$$

where H is the given altitude, \mathbf{V}_h is the horizontal wind, \mathbf{C} is the storm motion, and \mathbf{k} is the unit vector in the vertical

TABLE 1. Information on tornadoes associated with TC Yagi, with period C for 6–11.

No.	Province	City	Date	Time (BJT)	Lon (°E)	Lat (°N)
1	Jiangsu	Yangzhou	13 Aug 2018	0224	119.48	32.29
2	Tianjin	Jinghai	13 Aug 2018	1750	116.90	38.96
3	Jiangsu	Xuzhou	13 Aug 2018	1830	117.87	33.77
4	Anhui	Suzhou	13 Aug 2018	1900	117.95	33.62
5	Shandong	Zaozhuang	13 Aug 2018	2300	117.46	34.50
6	Shandong	Weifang	14 Aug 2018	1000	119.43	36.97
7	Shandong	Dongying	14 Aug 2018	1030	119.07	37.78
8	Shandong	Laizhou	14 Aug 2018	1030	120.12	37.35
9	Shandong	Binzhou	14 Aug 2018	1215	117.52	37.23
10	Shandong	Dongying	14 Aug 2018	1300	118.46	37.70
11	Shandong	Dezhou	14 Aug 2018	1330	117.41	37.67

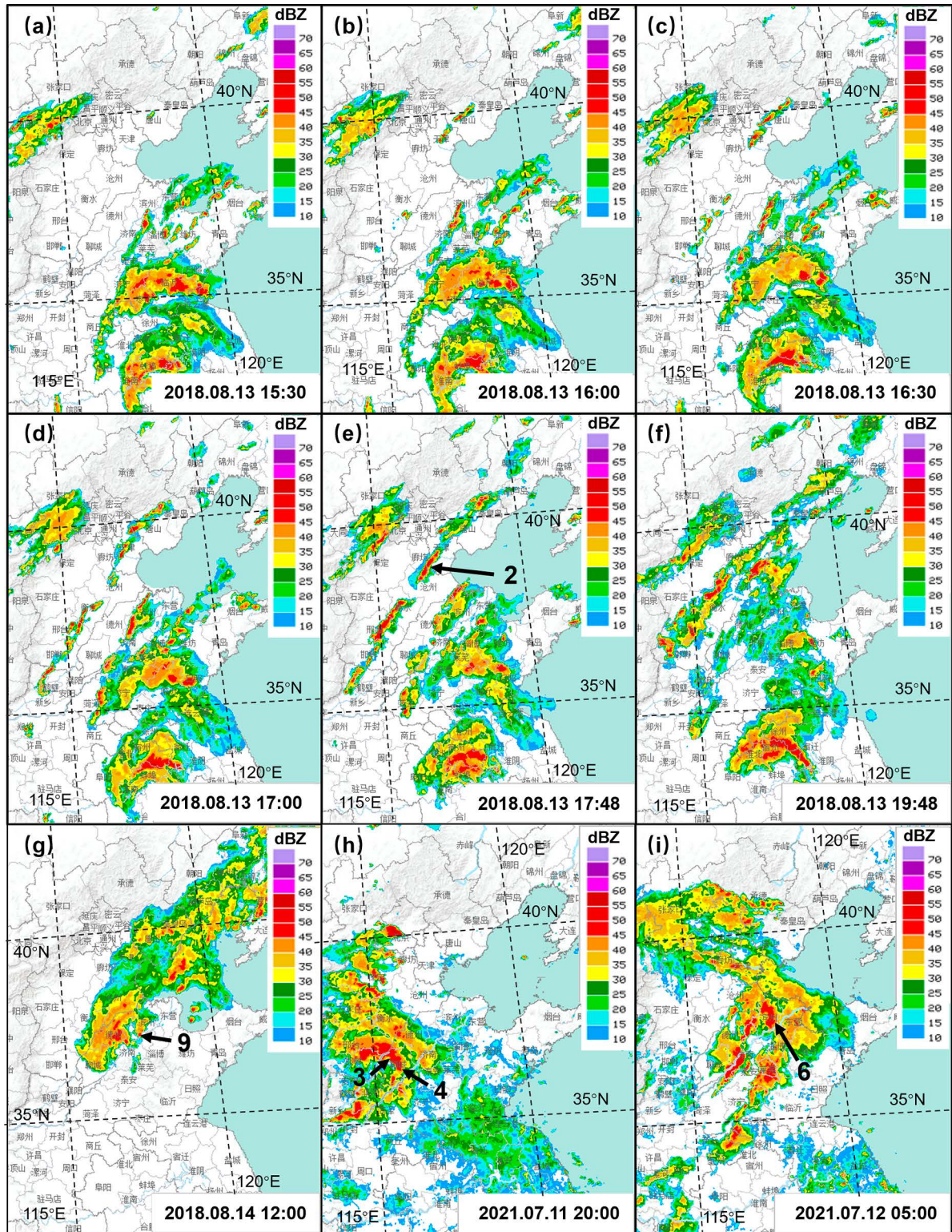


FIG. 2. Base reflectivity (dBZ) mosaics of TC Yagi at (a) 1530, (b) 1600, (c) 1630, (d) 1700, (e) 1748, and (f) 1948 BJT 13 Aug 2018, and (g) 1200 BJT 14 Aug 2018, and EC 711 at (h) 2000 BJT 11 Jul 2021 and (i) 0500 BJT 12 Jul 2021. The black arrows indicate the locations of tornadoes with the number label in black occurring at the panel time.

TABLE 2. MSLPs and maximum sustained surface winds of TC Yagi at tornadogenesis time.

Date	Time (BJT)	MSLP (hPa)	Max sustained surface winds (m s ⁻¹)
13 Aug 2018	Tornado 1 at 0200	990	20
13 Aug 2018	Tornadoes 2 and 3 at 1700	992	18
13 Aug 2018	Tornado 4 at 2000	994	18
13 Aug 2018	Tornado 5 at 2300	996	15
14 Aug 2018	Tornado 6 at 0800	998	13
14 Aug 2018	Tornadoes 7, 8, and 9 at 1100	998	13
14 Aug 2018	Tornadoes 10 and 11 at 1400	998	13

direction. In the present study, we will use SRH1 for which H is set equal to 1 km and the storm motion was estimated using the method of Bunkers et al. (2000).

The composite parameter STP was calculated following Thompson et al. (2003) using a mixed-layer method (also within the lowest 100 hPa):

$$\text{STP} = \frac{\text{MLCAPE}}{1000} \times \frac{\text{SHR6}}{20} \times \frac{\text{SRH1}}{100} \times \frac{(2000 - \text{MLLCL})}{1500}, \quad (4)$$

where MLLCL is the mixed layer lifting condensation level, and SHR6 is the magnitude of the bulk shear vector between 6 km and ground level. In this work, we also calculated the E-STP (Tochimoto et al. 2019) as follows:

$$\begin{aligned} \text{E-STP} = & \frac{\text{E-CAPE}}{1000} \times \frac{\text{MLCAPE}_{\max}}{\text{E-CAPE}_{\max}} \times \frac{\text{SHR6}}{20} \times \frac{\text{SRH1}}{100} \\ & \times \frac{(2000 - \text{MLLCL})}{1500}, \end{aligned} \quad (5)$$

where MLCAPE_{\max} (E-CAPE_{\max}) is the maximum value of MLCAP (E-CAPE) in the domain for calculation. The factor of $\text{MLCAPE}_{\max}/\text{E-CAPE}_{\max}$ was included in Eq. (5) in order to obtain a comparison between the distributions of STP and E-STP on an equitable basis, because E-CAPE is about 10 times smaller than MLCAP.

We also calculated the EHI that combines SRH1 with MLCAP as follows:

$$\text{EHI} = \frac{\text{SRH1} \times \text{MLCAPE}}{1.6 \times 10^5}. \quad (6)$$

Finally, we calculated the E-EHI (Tochimoto et al. 2019) as follows:

$$\text{E-EHI} = \frac{\text{SRH1} \times \text{E-CAPE}}{1.6 \times 10^5} \times \frac{\text{MLCAPE}_{\max}}{\text{E-CAPE}_{\max}}. \quad (7)$$

d. Classification of parent storms of tornadoes

In addition to individual radars, the mosaic of base reflectivities provided by the China Meteorological Administration was also used to show the big picture of TC and EC environments as well as their evolutions. The mosaic of base reflectivities is an optimal selection from the lowest three elevation

angles (i.e., 0.5°, 1.5° and 2.4°) (Bai et al. 2020a), which is also called a “terrain-based hybrid scan” (Fulton et al. 1998). In particular, the larger values from 1.5° to 2.4° elevation angles are used if the ratio of reflectivity area from 1.5° over 0.5° elevation angles is lower than a certain criterion. Otherwise, the larger value from 0.5° to 1.5° elevation angles is used. This method is to avoid large area of super refraction at the lowest elevation angle and/or to compensate beam blockage at lower elevation angles. The mosaic of base reflectivity had a spatial resolution of 1 km and a temporal resolution of 6 min.

The parent storms were classified into three types: the quasi-linear convective system (QLCS), cellular, and cluster types. The classification of the parent storm patterns was based on the morphology of their 40-dBZ base reflectivity contour at 0.5° elevation. First, when the length of the parent storm was equal to or longer than 100 km and the length was 3 times equal to or longer than the width, the parent storm was defined as a QLCS. Second, if the parent storm was discretely circular or elliptic and its length was less than 50 km, it was defined as a cellular storm. Finally, when the parent storm was not clearly identifiable as either a discrete cell or QLCS and its area was approximately 2500 km², it was delimited as a cluster.

3. Overview of the two cases

a. TC Yagi

TC Yagi formed in the western Pacific on 7 August 2018 and made landfall in Zhejiang Province, China, at 2300 Beijing time (BJT = UTC + 8 h, all times hereafter are in BJT) 12 August (Fig. 1a) with an MSLP of 985 hPa and a maximum sustained surface wind of 25 m s⁻¹. Less than 2 h after its landfall, it produced its first tornado in Yangzhou, Jiangsu Province (Fig. 1b, Table 1). While moving northward, Yagi produced the second tornado approximately eighteen hours after landfall in Tianjin city (Fig. 1b) about 700 km from TC center, which developed in association with an outer rainband of TC Yagi (Figs. 2a–f). Then, it generated another four tornadoes in the following 8 h in Jiangsu, Anhui, and Shandong Provinces (Fig. 1b). It is worth noting that after moving into Shandong Province at approximately 0500 BJT 14 August (Fig. 1a), TC Yagi continuously spawned six tornadoes within 3.5 h around noon from 1000 to 1330 BJT in northern Shandong Province (Fig. 1b), which is hereafter referred to as period C. This concentrated tornadogenesis period will be analyzed in detail in section 5. The MSLPs and sustained

TABLE 3. Information on tornadoes associated with EC 711, with period A for 1–5 and period B for 7–9.

No.	Province	City	Date	Time (BJT)	Lon (°E)	Lat (°N)
1	Shandong	Liaocheng	11 Jul 2021	1900	115.76	36.48
2	Shandong	Liaocheng	11 Jul 2021	1910–1930	115.69	36.25
3	Hebei	Xingtai	11 Jul 2021	1950	115.53	36.79
4	Shandong	Liaocheng	11 Jul 2021	2030	116.01	36.67
5	Shandong	Liaocheng	11 Jul 2021	2037–2058	116.08	36.80
6	Shandong	Binzhou	12 Jul 2021	0445	117.87	37.65
7	Shandong	Binzhou	12 Jul 2021	0545	118.05	37.89
8	Shandong	Binzhou	12 Jul 2021	0555	117.78	37.58
9	Shandong	Dongying	12 Jul 2021	0810	118.57	37.34
10	Shandong	Binzhou	12 Jul 2021	1420	117.65	37.66
11	Inner Mongolia	Hingan League	13 Jul 2021	1510–1550	122.91	46.73
12	Inner Mongolia	Xilingol League	13 Jul 2021	Afternoon	116.3	42.37
13	Inner Mongolia	Hulun Buir	13 Jul 2021	1700–1710	122.38	47.36

wind speeds of TC Yagi at the time of each tornadogenesis are given in Table 2. TC Yagi dissipated on 16 August without transforming into an EC. In total, TC Yagi produced 11 tornadoes (Fig. 1b; Table 1), the only TC tornado outbreak event in China to date.

b. EC 711

EC 711 formed in southeastern Shaanxi Province on 11 July 2021 and moved northeastward (Fig. 1c). It produced 13 tornadoes along its track in total (Fig. 1d; Table 3). This was the second and last tornado outbreak event in China to date. Similar to TC Yagi, EC 711 also had concentrated tornadogenesis periods but in the early evening and early morning rather than around noon. It continually spawned five tornadoes in western Shandong Province and southern Hebei

Province from 1900 to 2100 BJT 11 July (Figs. 1d and 2h), which is hereafter referred to as period A, and three tornadoes in northern Shandong Province from 0430 to 0600 BJT 12 July (Figs. 1d and 2i), which is hereafter referred to as period B. These two periods will be analyzed in section 5 in detail. Notably, the frequency of tornadoes (per unit time) was larger during periods A and C than during period B.

4. Characteristics of tornadoes and their parent storms in both events

a. Distribution of tornadoes

The spatial distributions of tornadoes relative to the cyclone centers differed. Both TC Yagi and EC 711 produced

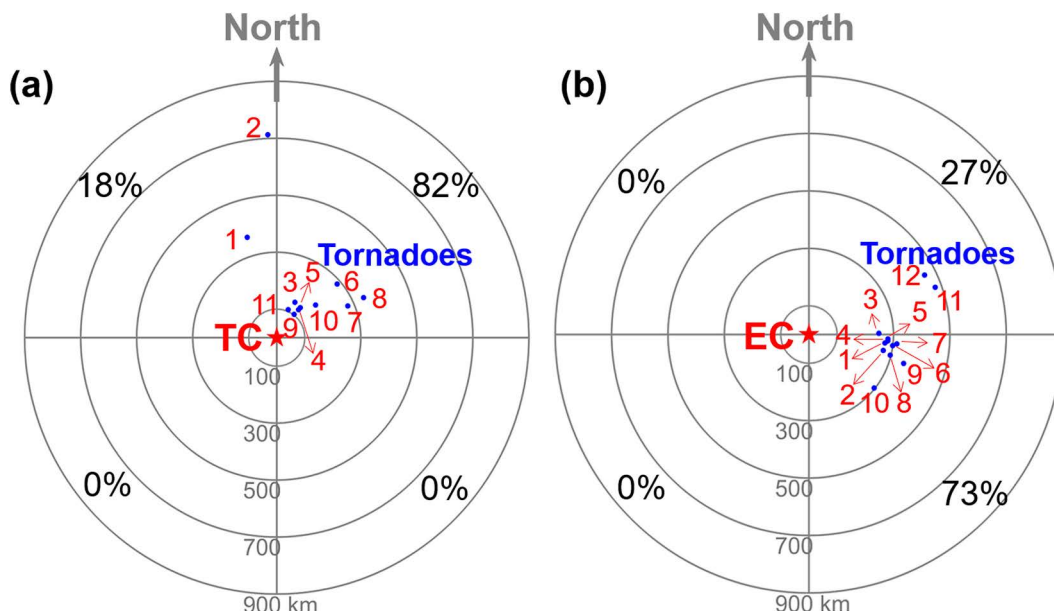


FIG. 3. (a) Locations of tornadoes (blue dots) associated with TC Yagi relative to the center of their parent TC (star) at the time of each tornadogenesis in Earth-relative coordinates, denoted by the number labels (red) as listed in Table 1. (b) As in (a), but for EC 711 with the number labels (red) as listed in Table 3. The percentage of tornadoes that occurred in each quadrant is also given.

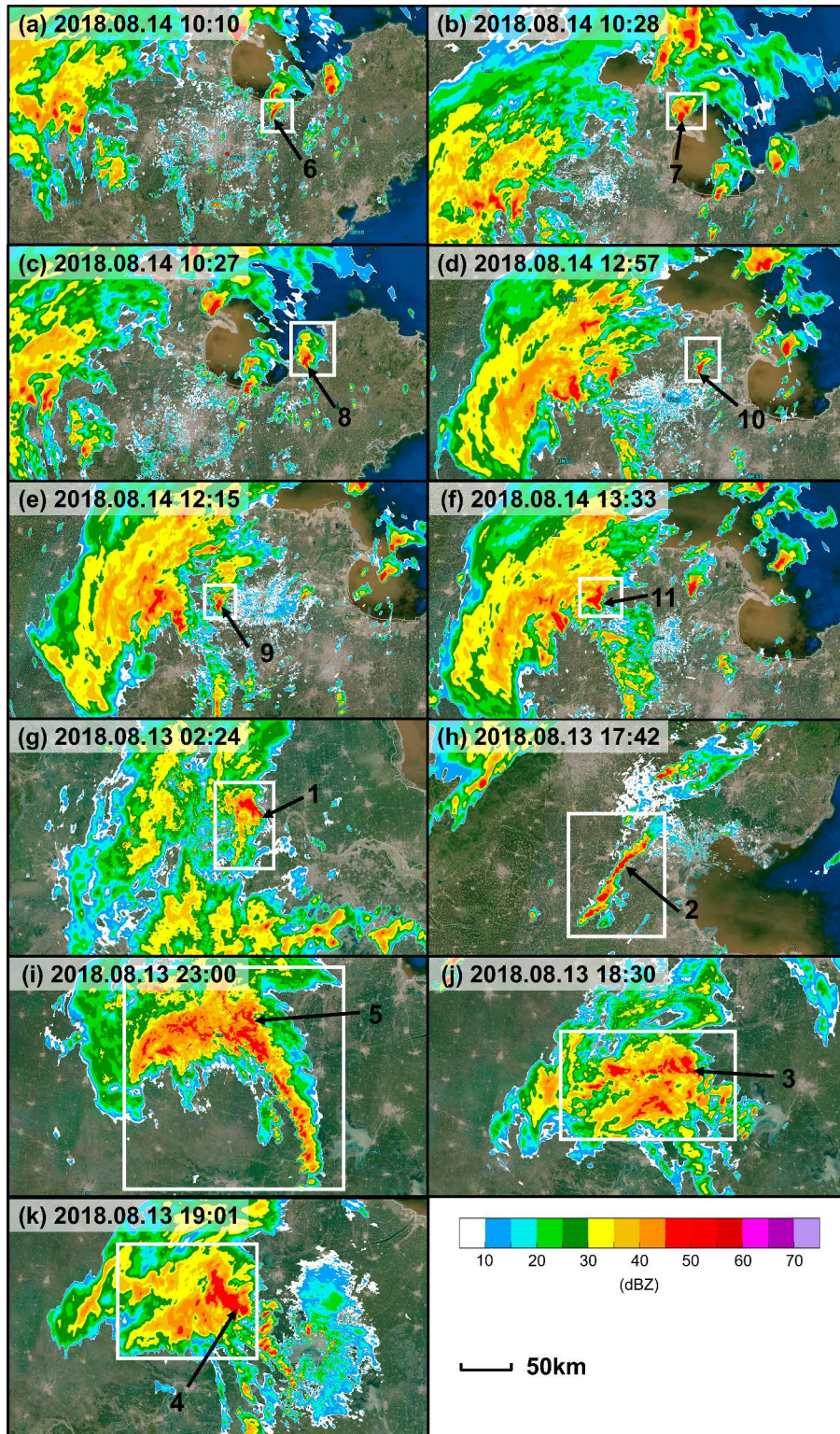


FIG. 4. Radar reflectivity (dBZ) at 0.5° elevation for all the parent storms (denoted by the white rectangles) of tornadoes in TC Yagi. The positions of each tornado with the number label in black are denoted by the black arrows.

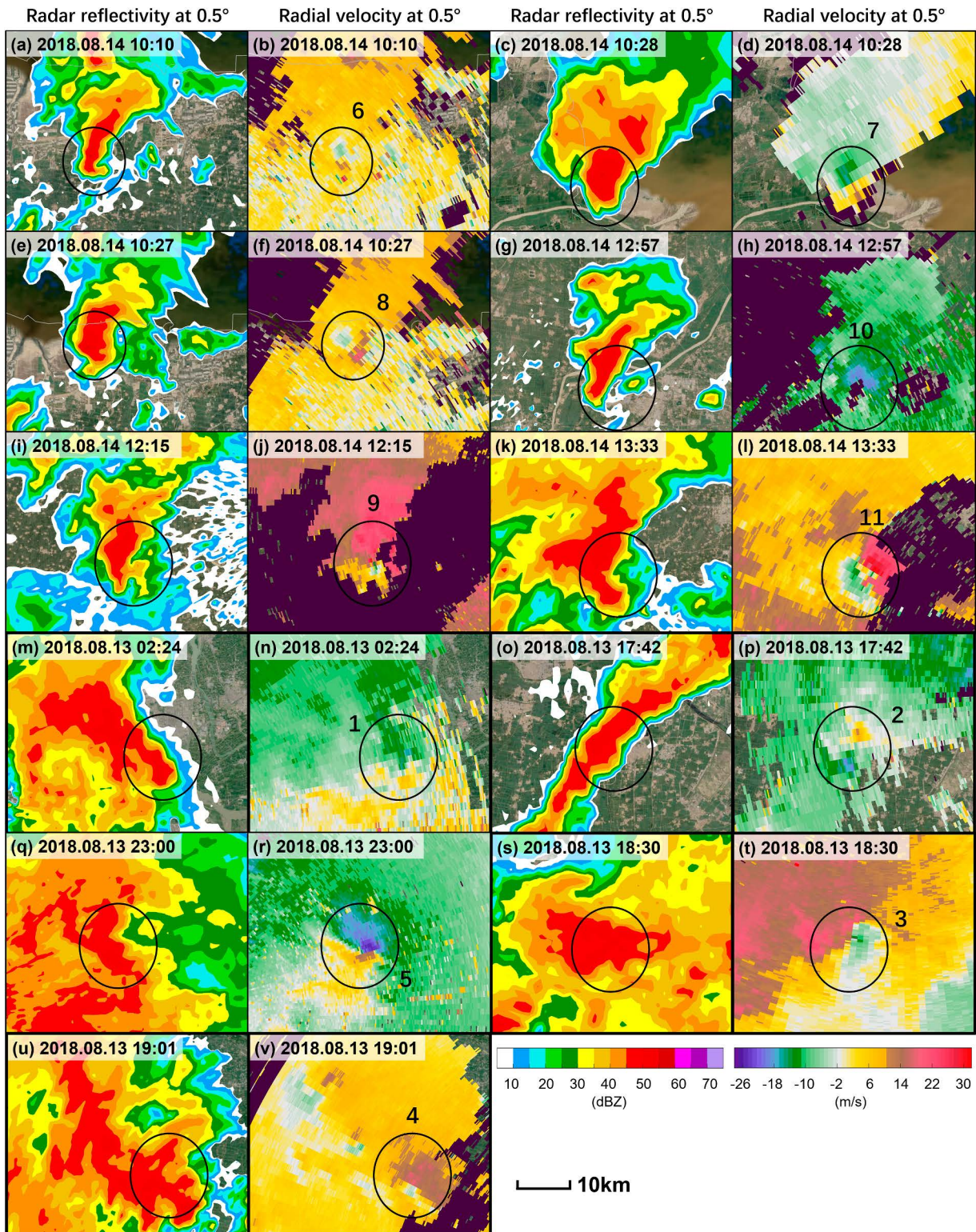


FIG. 5. Enlarged view of radar reflectivity (dBZ) and radial velocity ($m s^{-1}$) at 0.5° elevation around each tornado shown in Fig. 4 for TC Yagi.

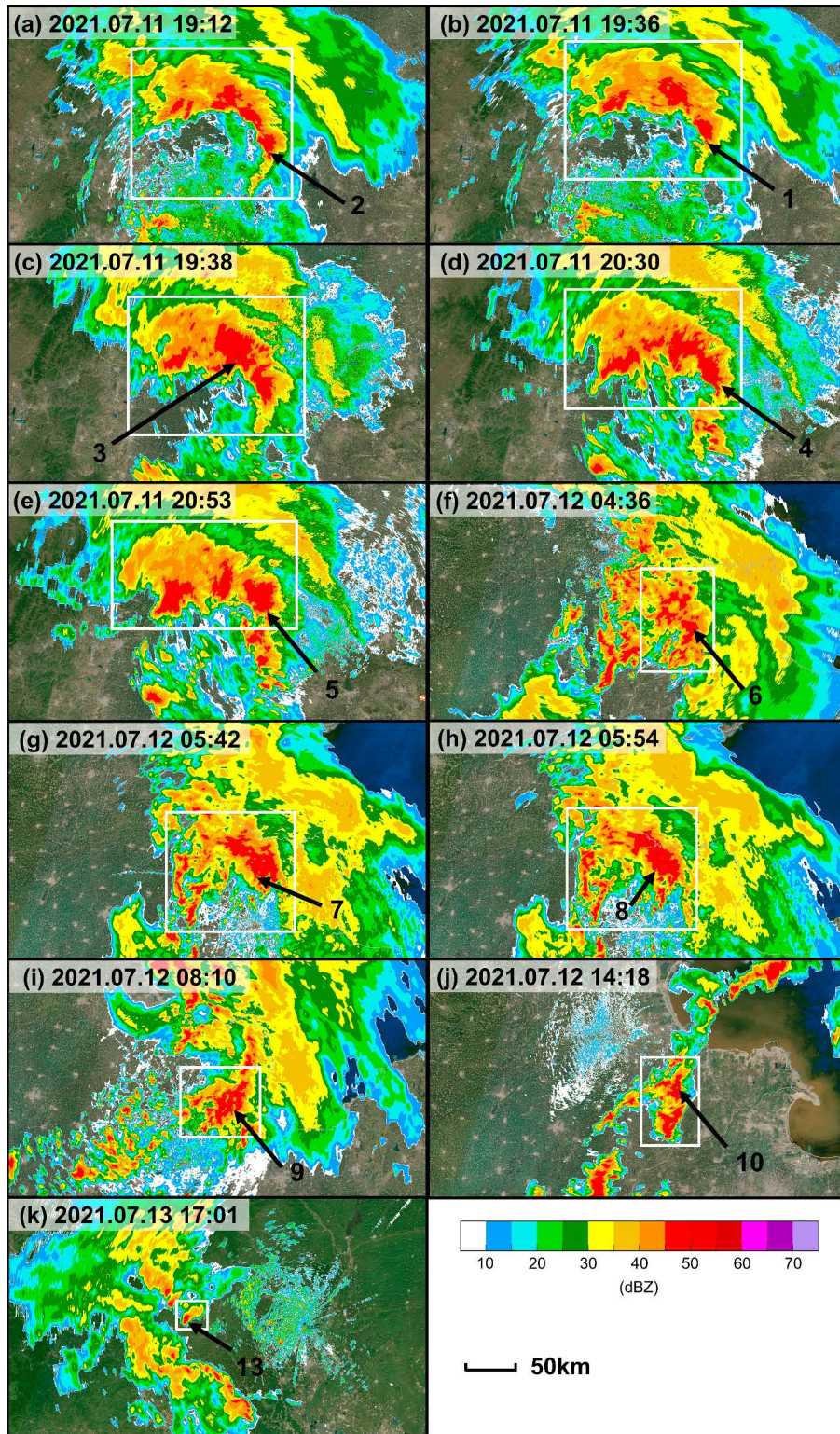


FIG. 6. As in Fig. 4, but for EC 711.

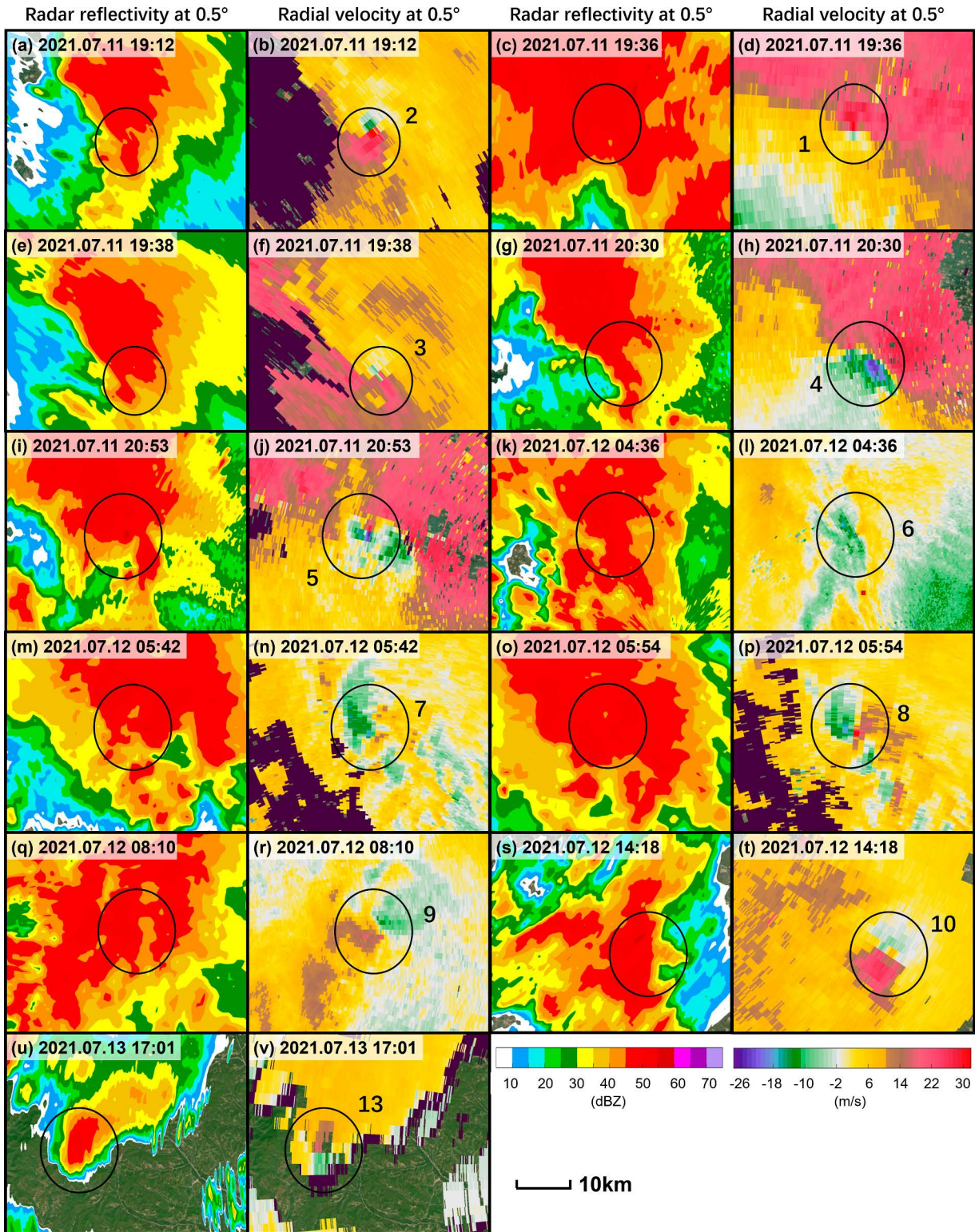


FIG. 7. Enlarged view of radar reflectivity (dBZ) and radial velocity (m s⁻¹) at 0.5° elevation around each tornado shown in Fig. 6 for EC 711.

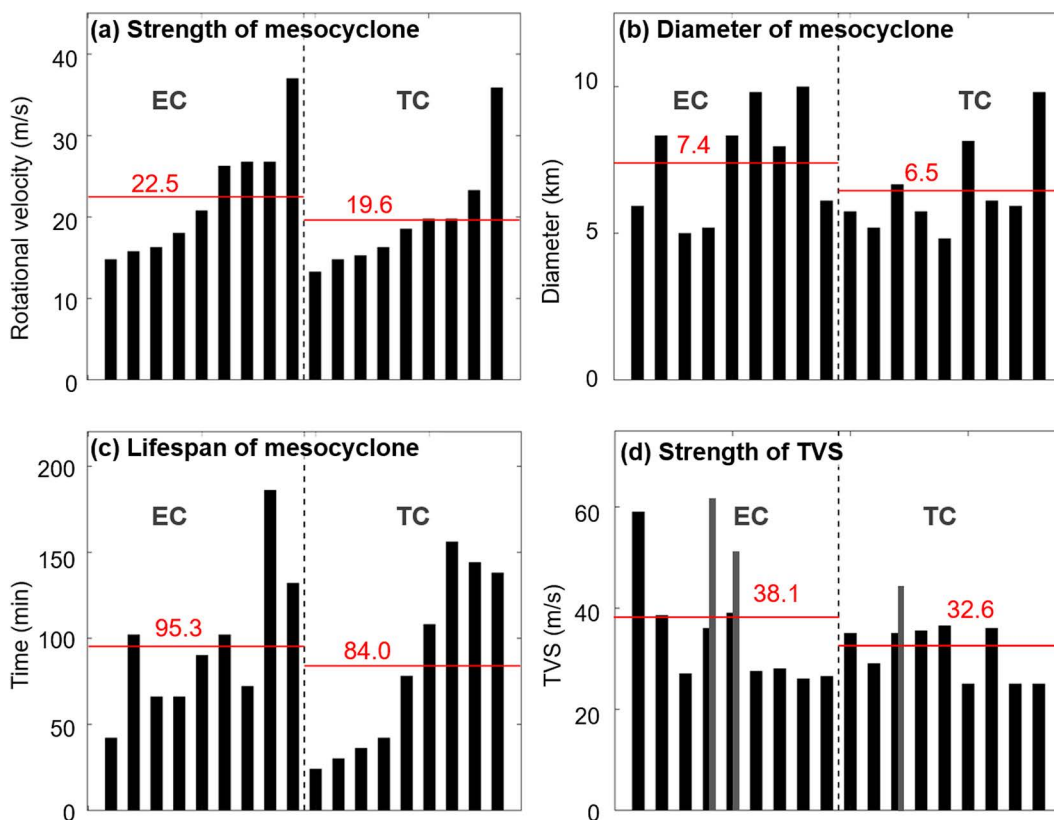


FIG. 8. Maximum (a) rotational velocity (m s^{-1}) and (b) diameter (km) of tornadic mesocyclones at 0.5° elevation in (c) their whole life span, for (left) EC 711 and (right) TC Yagi. (d) The maximum strength (m s^{-1}) of the identified TVS of each tornado. The red lines indicate the mean values. Bars are arranged in ascending order based on the maximum strength of the mesocyclone, while TVS bars in (d) that correspond to one mesocyclone bar are plotted using adjacent narrower black and gray bars.

most tornadoes in the eastern sections of the cyclones. However, TC Yagi generated most tornadoes in the northeast quadrant (Fig. 3a), similar to the general features of TC tornadoes in China (Bai et al. 2020b), while EC 711 generated most tornadoes in the southeast quadrant (Fig. 3b), consistent with statistical results obtained for EC tornado outbreaks in the United States (e.g., Johns and Doswell 1992; Tochimoto and Niino 2016).

b. Characteristics of parent storms of tornadoes

Striking distinctions were observed in the parent storms of tornadoes between EC 711 and TC Yagi. Figure 2 shows the radar mosaics of basic reflectivities for EC 711 over the two concentrated tornadogenesis periods at 2000 BJT 11 July 2021 (Fig. 2h) and 0500 BJT 12 July 2021 (Fig. 2i), as well as for TC Yagi over the concentrated tornadogenesis period at 1200 BJT 14 August 2018 (Fig. 2g). More apparent band features were observed in EC 711 than in TC Yagi. Most tornadoes associated with TC Yagi were generated in discrete minisupercells (Figs. 4 and 5), which are equivalent to the discrete right-moving (RM) mode according to the classification by Thompson et al. (2012), while most tornadoes in EC 711 were spawned from supercells in quasilinear

convective systems (QLCSs) and clusters (Figs. 6 and 7), which are equivalent to the line RM or cluster RM modes according to the classification by Thompson et al. (2012). Out of the 11 tornadoes in TC Yagi, 7 were generated in discrete cellular minisupercells (Figs. 4a–g), and 2 were generated in minisupercells embedded in QLCSs (Figs. 4h,i), while 2 were associated with clusters (Figs. 4j,k). However, for EC 711, except for 2 tornadoes (T11 and T12) in inner Mongolia whose parent storms were not covered by radar data, 5 out of the remaining 11 tornadoes were spawned by supercells embedded in QLCSs (Figs. 6a–e), 5 were spawned by supercells in clusters (Figs. 6f–j), and only 1 was spawned by a cellular supercell (Fig. 6k).

Distinct differences also existed in the strengths, life spans, and diameters of mesocyclones and strength of tornado vortex signatures (TVSs) between EC 711 and TC Yagi. The mesocyclones associated with tornadoes in EC 711 had larger mean maximum rotational velocities and diameters than those in TC Yagi (Figs. 8a,b). The average rotational velocities of mesocyclones associated with tornadoes in EC 711 and TC Yagi were 22.5 and 19.6 m s^{-1} (Fig. 8a), respectively. The mesocyclones associated with tornadoes in EC 711 had a mean diameter of 7.4 km, which was ~ 1 km larger than that

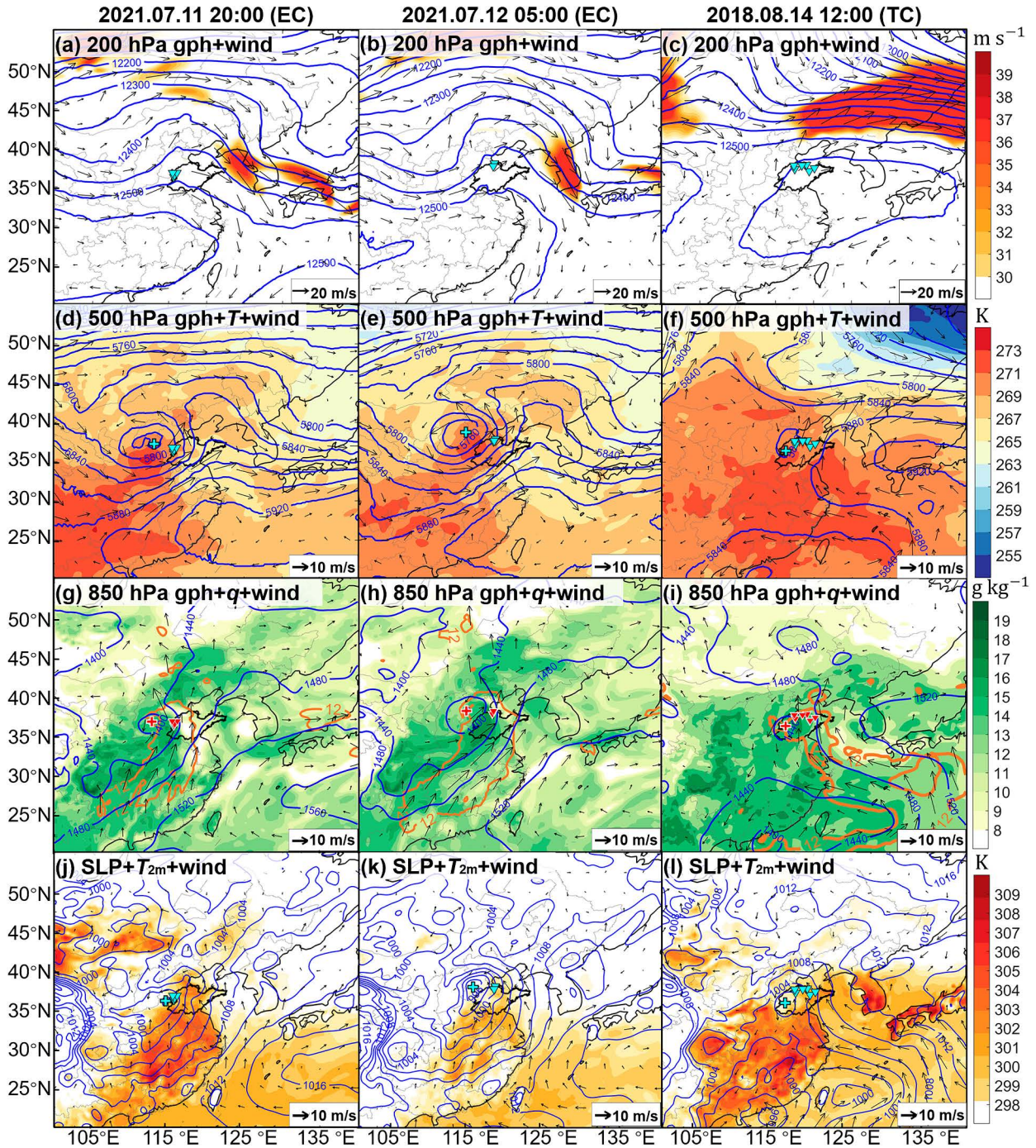


FIG. 9. (a)–(c) Geopotential height (contour; gpm), wind (vectors; $m s^{-1}$), and upper-level jet (shaded with the wind speed larger than $30 m s^{-1}$) at 200 hPa; (d)–(f) geopotential height (contours; gpm), wind (vectors; $m s^{-1}$), and temperature (shaded; K) at 500 hPa; (g)–(i) geopotential height (contours; gpm), wind (vectors; $m s^{-1}$), and low-level jet with wind speed of beyond $12 m s^{-1}$ (orange contour) at 850 hPa; (j)–(l) SLP (contours; hPa), 2-m temperature (shaded; K), and 10-m wind (vectors; $m s^{-1}$) at (left) 2000 BJT 11 Jul 2021, (center) 0500 BJT 12 Jul 2021, and (right) 1200 BJT 14 Aug 2018. The triangles pointing down indicate the positions of tornadoes, and the crosses indicate the cyclone center at the respective levels. The boundary of Shandong Province is highlighted in black lines.

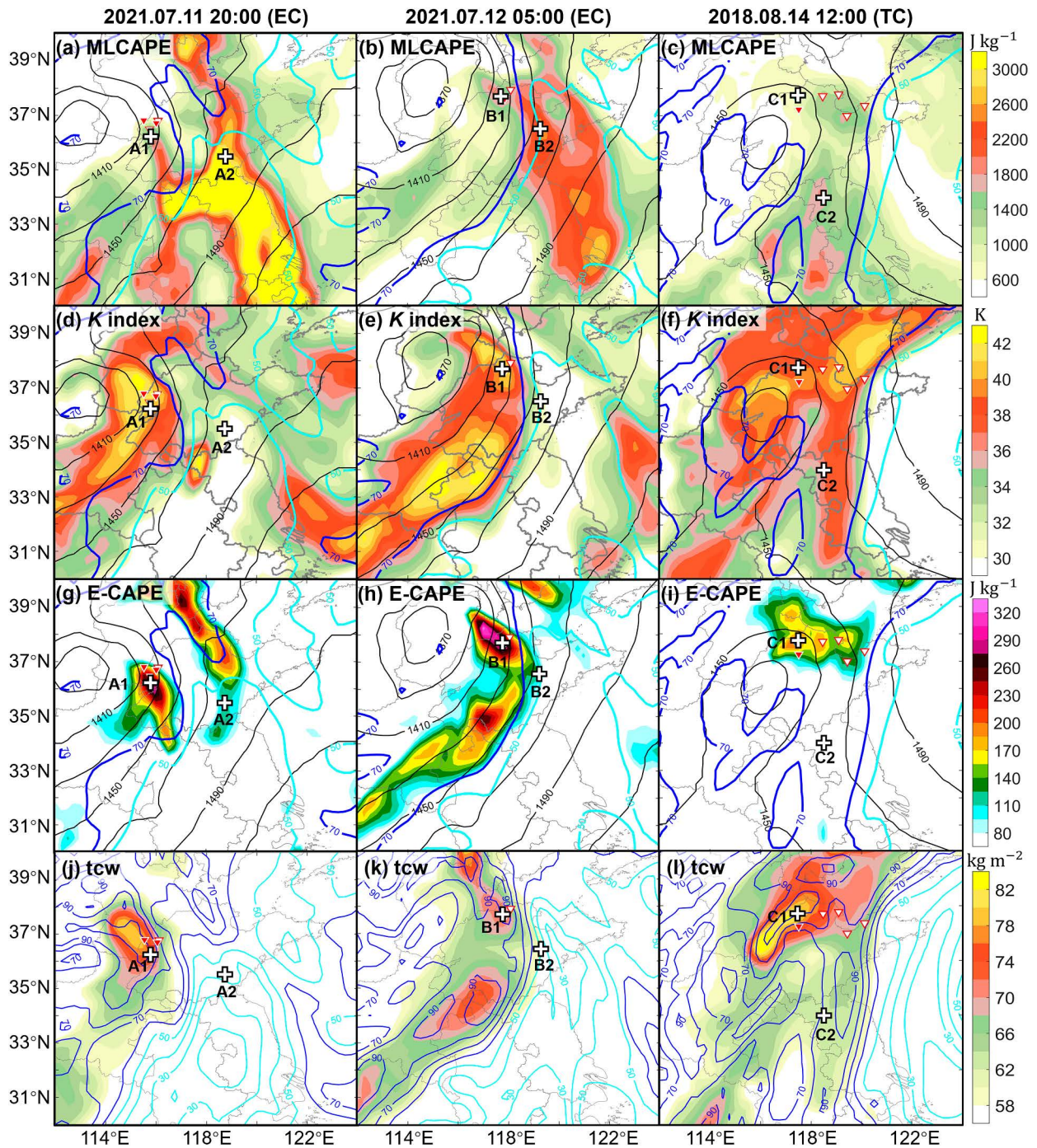


FIG. 10. (a)–(c) MLCAPE (shaded; J kg^{-1}), (d)–(f) the K index (shaded; K), (g)–(i) E-CAPE (shaded; J kg^{-1}), and (j)–(l) total column water (tcw; shaded; kg m^{-2}) and relative humidity (blue contour for $\text{RH} > 50\%$ and cyan contour for $\text{RH} \leq 50\%$) at 700 hPa for EC 711 (left) over period A at 2000 BJT 11 Jul 2021 and (center) over period B at 0500 BJT 12 Jul 2021, and (right) for TC Yagi over period C at 1200 BJT 14 Aug 2018. The black, cyan, and blue contours in the top three rows denote geopotential height (gpm) at 850 hPa and RH of 50% and 70% at 700 hPa, respectively. The triangles pointing down indicate the tornadoes occurring during each period with the red-filled ones denoting the tornadoes occurring at the panel time. The cross marks at A1, A2, B1, B2, C1, and C2 denote the locations of skew T -diagrams plotted in Fig. 11.

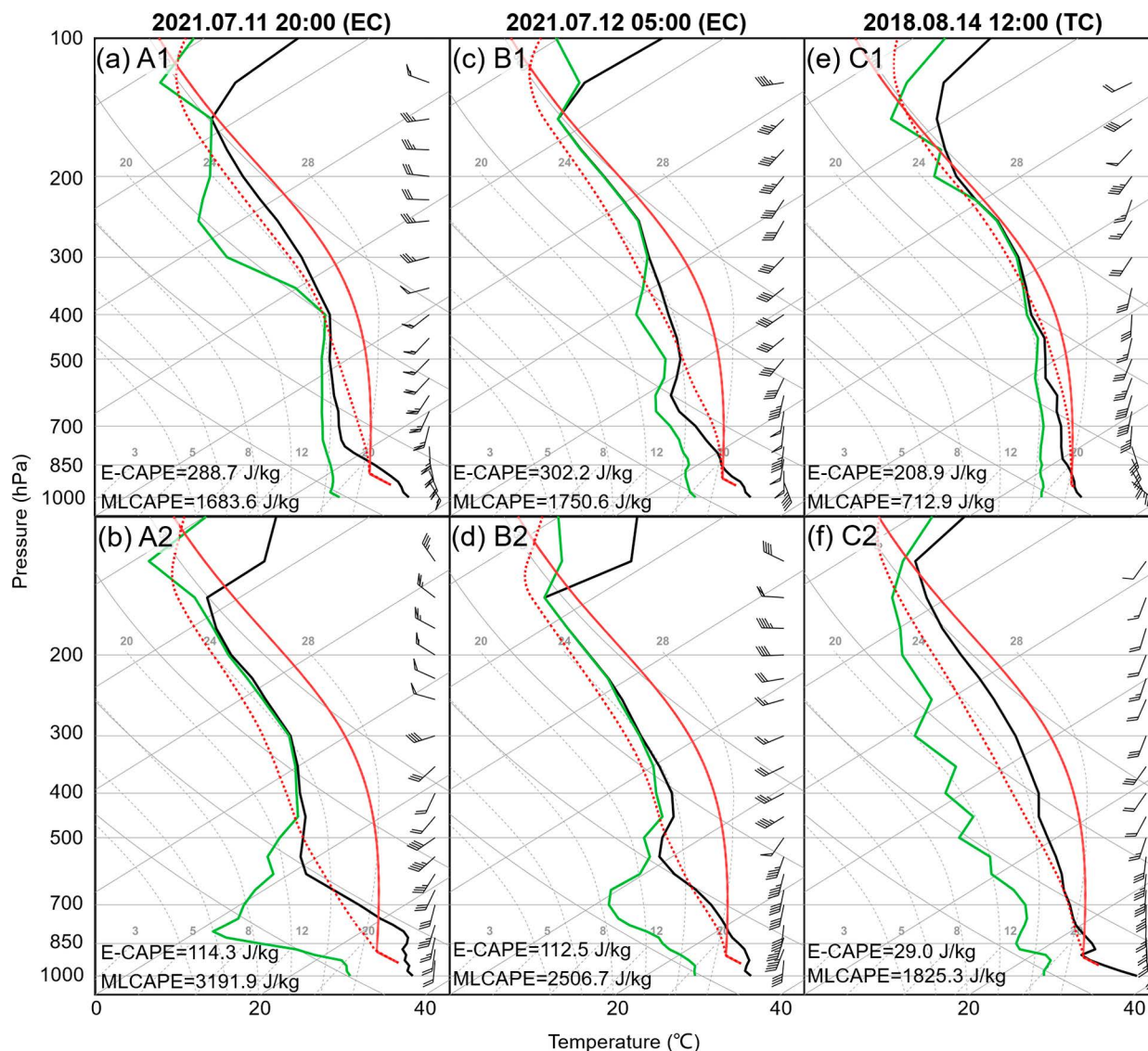


FIG. 11. Skew T diagrams at (a) A1 and (b) A2 at 2000 BJT 11 Jul 2021 for period A, (c) B1 and (d) B2 at 0500 BJT 12 Jul 2021 for period B, and (e) C1 and (f) C2 at 1200 BJT 14 Aug 2018 for period C. Half barbs, full barbs, and pennants represent 2, 4, and 20 m s^{-1} , respectively. The locations of A1, A2, B1, B2, C1, and C2 are given in Fig. 10. The red solid line denotes the lapse rate for a mixed layer parcel, while the red dotted line denotes the lapse rate for a mixed layer parcel considering the entrainment. Values of MLCAPE and E-CAPE are also given in the bottom-left corners.

in TC Yagi (Fig. 8b). In addition, the mean life span of the mesocyclones associated with tornadoes in EC 711 was longer than that in TC Yagi (95.3 versus 84.0 min, Fig. 8c). Likely due to the stronger mesocyclones, the TVSSs in EC 711 were stronger than those in TC Yagi. The average intensities of TVSSs while generating tornadoes in EC 711 and TC Yagi were 38.1 and 32.6 m s^{-1} , respectively (Fig. 8d). The sample of mesocyclones and TVSSs in EC 711 was not biased closer to the radars than for TC Yagi case. The mean distance for mesocyclones at their maximum strength times was both 76 km for EC 711 and TC Yagi. The mean distance for TVSSs at their maximum strength times was 72 km for EC 711 and 73 km for TC Yagi.

5. Environmental features

This section compares the environmental features and the convective parameters associated with the tornado generation of TC Yagi with those of EC 711. As described in section 4a, EC 711 generated tornadoes mainly in periods A and B, while TC Yagi produced tornadoes mainly in period C, with periods A and C having larger tornado frequencies than period B. Owing to the small changes in environmental features and convective parameters within each of these periods, the middle moment of each period was selected to represent the entire period; these moments were 2000 BJT 11 July 2021, 0500 BJT 12 July 2021, and 1200 BJT 14 August 2018 for periods A, B, and C, respectively.

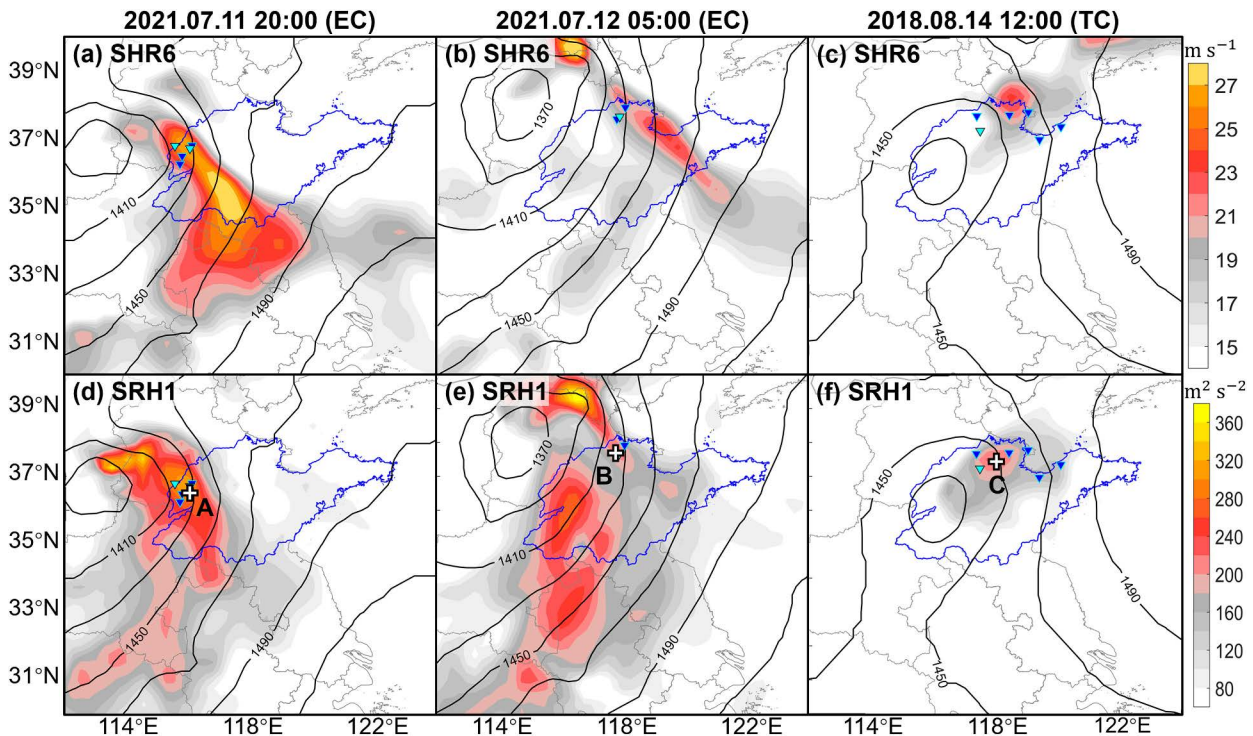


FIG. 12. (a)–(c) SHR6 (shaded; m s^{-1}) and (d)–(f) SRH1 (shaded; $\text{m}^2 \text{s}^{-2}$) as well as geopotential height (contours; gpm) at 850 hPa at (left) 2000 BJT 11 Jul 2021 for period A, (center) 0500 BJT 12 Jul 2021 for period B, and (right) 1200 BJT 14 Aug 2018 for period C. The triangles pointing down indicate the tornadoes occurring during each period with the cyan ones denoting the tornadoes occurring at the panel time. The cross marks at A, B, and C, respectively, in (d), (e), and (f) denote the locations of hodograph diagrams plotted in Fig. 13.

a. Synoptic features

During period A, the EC was centered over Shanxi Province (Fig. 9d) at 500 hPa with a short-wave trough extending from the EC center to the southwest. The subtropical high was situated at approximately 25°N with a long ridge extending northward along the eastern coastal area of China, which led to strong southwesterly wind at 500 hPa in the tornadogenesis area between the EC center and subtropical high. This strong southwesterly wind appeared as a strong low-level southwesterly jet at 850 hPa (Fig. 9g), advecting warm moist air from the south to western Shandong Province. The EC center had an MSLP of 998 hPa and was located to the southeast of the 500-hPa EC center (Fig. 9j), producing southeasterly wind at surface in the tornadogenesis area and thus strong vertical shear over Shandong Province working together with the strong southwesterly wind at 500 hPa. During period B, the EC apparently intensified both at 500 hPa and at the surface (Figs. 9e,k). With the extratropical cyclone shifting to the east and intensifying, the low-level southwesterly jet extended both northeastward and southwestward (Fig. 9h). This is a synoptic pattern typical of EC tornado outbreaks, as has been observed in the United States (e.g., Johns and Doswell 1992; Tochimoto and Niino 2016; Tochimoto et al. 2019).

During period C for the TC Yagi situation, the cyclone was located over northern Shandong Province, slightly to the east of the EC center in the above EC tornado outbreak event but

much smaller and weaker than the EC, especially at upper levels (Figs. 9f,i,l). The SLP at the TC center was 1000 hPa (Fig. 9l). The near-surface wind in Shandong Province was southeasterly, with a similar direction and speed as that in the EC case. However, at 500 hPa, there was only one closed geopotential height contour around the TC center. The TC experienced a recurring process with short-wave trough at 500 hPa located far to the north in inner Mongolia (Fig. 9f) and a subtropical high situated at $\sim 35^\circ\text{N}$, which was approximately 10° north of that in the EC case. The center of the subtropical high was almost at the same latitude as that of the TC center, producing roughly southerly rather than southwesterly wind over Shandong Province. The low-level jet at 850 hPa had a similar speed as that in the EC case but with a greater longitudinal component over Shandong Province (Fig. 9i), extending from the southeast along the southern edge of the subtropical high rather than southwest as in the EC case. Consequently, less veering wind features were observed in the lower part of the troposphere in the TC case. Distinct from the EC case, a very strong upper-level jet streak existed at 200 hPa between the westerly trough and the subtropical high to the north of the TC, with Shandong Province located on the right of the jet entrance (Fig. 9c), facilitating upper-level divergence; this may have enhanced synoptic-scale lifting and was thus favorable for convection development. The synoptic pattern of this TC tornado outbreak event was also quite typical of TC tornado outbreaks reported in the literature (e.g., Cohen 2010; Verbout et al. 2007).

b. Environmental parameters

Environmental parameters, including MLCAPE, E-CAPE, K index, SRH1, 0–6-km SHR (SHR6), STP, E-STP, EHI, and E-EHI, at the middle moments of the three concentrated tornadogenesis periods of the two tornado outbreaks are analyzed and compared in this section.

1) THERMODYNAMIC PARAMETERS

The environment of EC 711 is more unstable than that of TC Yagi, with the largest instability observed over period A for EC 711, followed by in period B for EC 711 and then in period C for TC Yagi. Both of the concentrated tornadogenesis periods of EC 711 showed larger MLCAPE values than period C of TC Yagi. Over period A, a region of large MLCAPE values exceeding 3000 J kg^{-1} existed southeast of the EC center, extending southward for at least 500 km (Fig. 10a). Over period B, the MLCAPE distribution was similar to that over period A but with a smaller maximum value of approximately 2700 J kg^{-1} (Fig. 10b). MLCAPE over period C for TC Yagi was notably smaller than that of EC 711, with the largest value of approximately 2200 J kg^{-1} existing south of TC Yagi, south of Shandong Province (Fig. 10c). Similar to previous findings (Sueki and Niino 2016; Bai et al. 2020b; Tochimoto et al. 2019; Bai 2021), the large MLCAPE values were not collocated well with the locations of tornadoes over all three periods in either event.

Relative to MLCAPE, better collocation was found between the large K index and high-tornado-density area in all three periods. The largest K index was observed in the region of tornadogenesis over period A, with a maximum value of 43.2 K (Fig. 10d), followed by period B and period C, with maximum values of 42.8 and 41.6 K, respectively (Figs. 10e,f). Consistent with the results of Sueki and Niino (2016), Tochimoto et al. (2019) and Bai et al. (2020b), E-CAPE showed a much better collocation with the positions of tornadoes than MLCAPE for both EC 711 and TC Yagi events. Periods B and A for EC 711 had maximum E-CAPE values of 320 and 275 J kg^{-1} with a 40% entraining rate (Figs. 10g,h), much larger than that in period C for TC Yagi at approximately 180 J kg^{-1} (Fig. 10i).

The better skills of E-CAPE and the K index than MLCAPE were mainly due to moister air at midlevels in their high value area. The distribution of total column water and relative humidity at 700 hPa were quite consistent with those of K index and E-CAPE (Figs. 10j–l). A comparison between the derived sounding at high E-CAPE locations (A1, B1, and C1 in Figs. 10g,h,i) with high MLCAPE locations (A2, B2, and C2 in Figs. 10a–c) shows that high E-CAPE locations were mainly due to higher moisture as revealed by higher mid-level relative humidity and thus less decreased potential energy due to entrainment (Figs. 11a,c,e), while high MLCAPE locations, which mainly resulted from larger lapse rate due to drier environment, suffered much more decrease of potential energy and thus smaller E-CAPE (Figs. 11b,d,f). This feature has been also demonstrated for tornado outbreak potentials in both tropical cyclone (Sueki and Niino 2016) and extratropical cyclone (Tochimoto et al. 2019) environments.

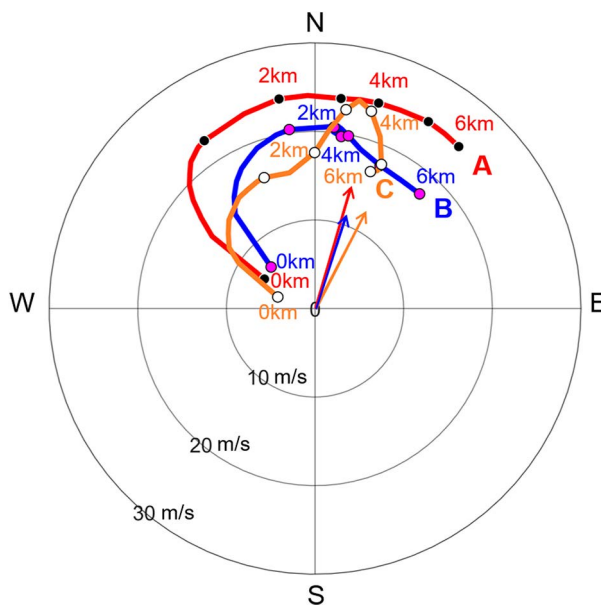


FIG. 13. Hodograph at the locations of A, B, and C given in Figs. 12d–f. The solid dots indicate 0, 1, 2, 3, 4, 5, and 6 km AGL. The estimated storm motions using the method of Bunkers et al. (2000) are also shown with arrows.

2) DYNAMIC PARAMETERS

SHR6 is a dynamic parameter that is usually used to determine convection organization, and an SHR6 value larger than 20 m s^{-1} is favorable for supercell formation (Markowski and Richardson 2010). Analyses of the synoptic flow in section 5a suggested a larger vertical shear in EC 711 due to its baroclinic features. The largest SHR6 value over period A for EC 711 in the area of tornadogenesis was larger than 20 m s^{-1} (Fig. 12a), while the largest SHR6 value in the region of tornadogenesis in northern Shandong Province was less than 20 m s^{-1} over period B of EC 711 and over period C of TC Yagi (Figs. 12b,c). Consequently, period A of EC 711 provided a kinematically much more favorable environment for supercell and tornadogenesis than period B of EC 711 or period C of TC Yagi.

SRH1 is an important parameter conducive to tornadogenesis. High-tornado-density areas were generally located in areas with large SRH1 values, but the collocations between the tornado centers and maximum values differed between the two events. The maximum SRH1 value of EC 711 was obviously larger than that in TC Yagi but did not match the high-density area of tornadoes as well as that in TC Yagi. Over period A for EC 711, the region of tornadogenesis was collocated with the area with a submaximum SRH1 surpassing $260 \text{ m}^2 \text{ s}^{-2}$ in western Shandong Province (Fig. 12d). Over period B for EC 711, the maximum SRH1 shifted north of the tornadogenesis area, and the SRH1 over the region of tornadogenesis was only slightly larger than $200 \text{ m}^2 \text{ s}^{-2}$ (Fig. 12e), much smaller than that over period A. Over period C for TC Yagi, the maximum SRH1 was better collocated with the region of tornadogenesis, with a value slightly exceeding $200 \text{ m}^2 \text{ s}^{-2}$.

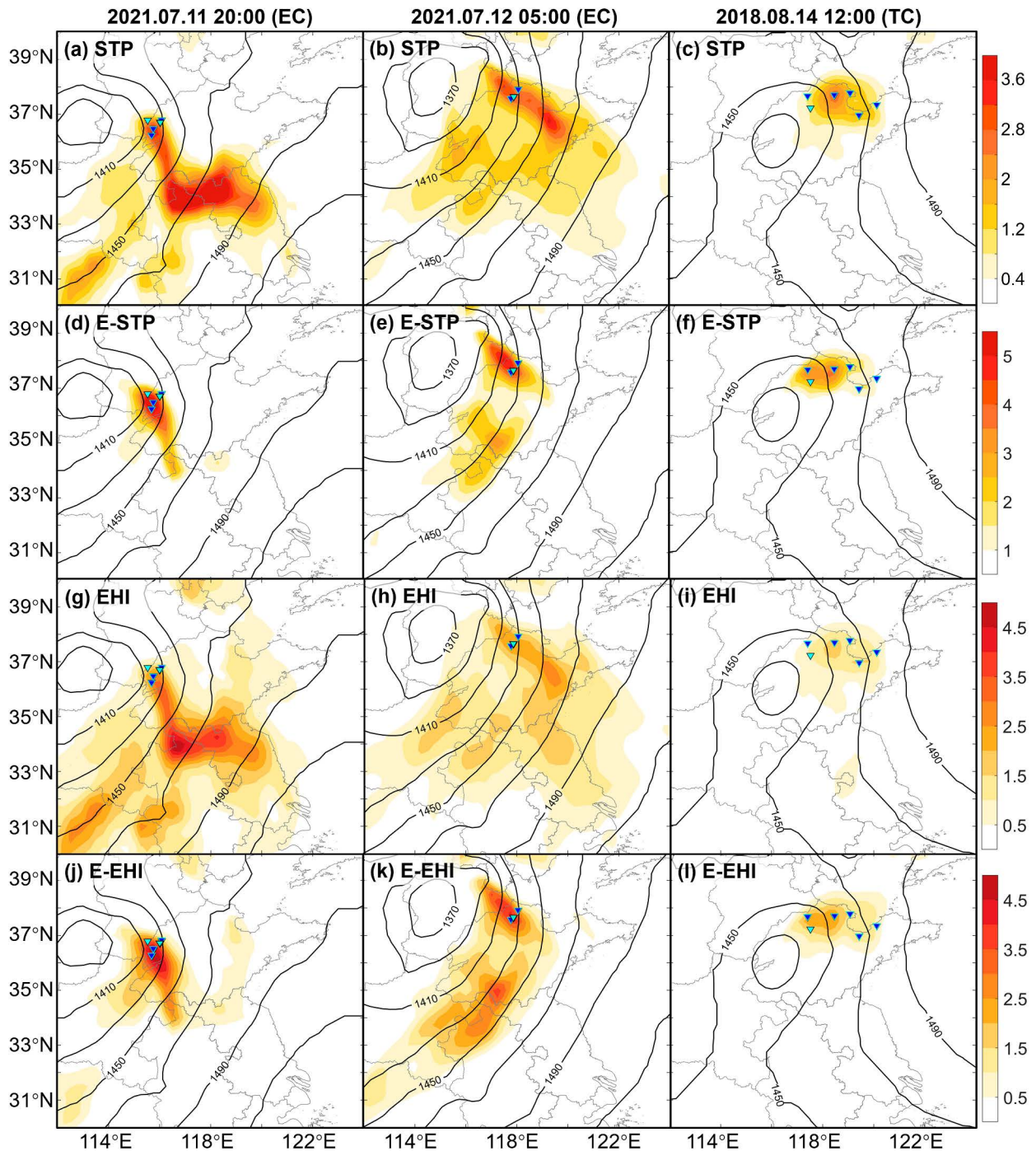


FIG. 14. (a)–(c) STP (shaded), (d)–(f) E-STP (shaded), (g)–(i) EHI (shaded), and (j)–(l) E-EHI (shaded) as well as geopotential height (contours; gpm) at 850 hPa (left) at 2000 BJT 11 Jul 2021 for period A, (center) at 0500 BJT 12 Jul 2021 for period B, and (right) at 1200 BJT 14 Aug 2018 for period C. The triangles pointing down indicate the tornadoes occurring during each period with the cyan ones denoting the tornadoes occurring at the panel time.

(Fig. 12f). These results show that either SHR6 or SRH1 did not collocate with tornado outbreak region as well as E-CAPE, especially in the EC 711 event.

The differences in the distributions of dynamic parameters between EC 711 and TC Yagi were possibly due to different

features of EC and TC. Hodographs near the centers of the high-tornado-density areas show that all three periods featured veering low-level winds, with larger SRH1 and SHR6 with more apparently veering pattern observed in periods A and B than C (Fig. 13). The near-surface winds of EC 711

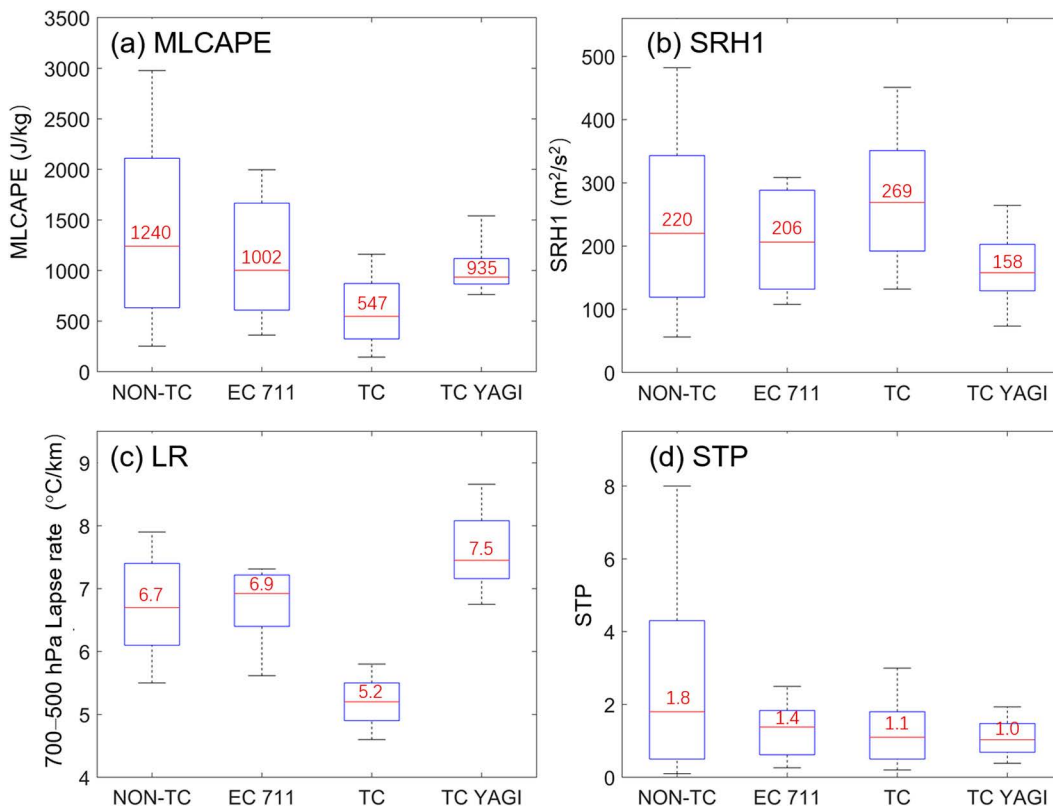


FIG. 15. Box-and-whisker diagrams, where percentile extents represent 25th–75th for boxes, 10th–90th for whiskers, and 50th at the bar in the box, for (a) MLCAPE (J kg^{-1}), (b) SRH1 ($\text{m}^2 \text{s}^{-2}$), (c) 700–500-hPa lapse rate ($^{\circ}\text{C km}^{-1}$), and (d) STP. The NON-TC and TC denote the statistics for non-TC and TC tornado outbreak events adapted from Fig. 8 of Edwards et al. (2012).

over both periods A and B were similar to that of TC Yagi over period C. However, the winds at 1 and 6 km above ground level were apparently different between EC 711 and TC Yagi. Due to the larger baroclinicity of EC, the cyclone center tilted northward with height (Figs. 9d,g,j), making the tornado outbreak locations shift from the northeast quadrant near the surface to the east at 850 hPa and to the southeast quadrant at 500 hPa. As a result, the winds at the tornado outbreak locations changed from southeasterly wind near the surface to southerly at 850 hPa and to the southwesterly at 500 hPa, producing apparent veering wind shear. However, in TC Yagi event, the cyclone center did not change much at different levels due to its approximately barotropic feature (Figs. 9f,i,l) and weaker environmental vertical shear (Figs. 12a–c), likely resulting from being farther from short-wave trough relative to EC 711. As a result, similar wind directions at different levels and thus less veering extent were observed near the tornado locations. In addition to the differences in the wind directions, the much stronger EC than TC produced much stronger winds from 1 to 6 km above ground level (Figs. 9d,e,f). Consequently, EC 711 had much larger SHR6 and SRH1 than TC Yagi. The larger differences in the wind especially in the wind directions at different levels in the EC event might have caused the location of maximum SHR6 (Figs. 12a,b) to be displaced

from the location of maximum total column water (Figs. 10j,k), and thus the poor collocation between the E-CAPE and SHR6.

3) COMPOSITE PARAMETERS

Because of the notable differences in the distributions of MLCAPE, E-CAPE, SHR6, and SRH1, the distributions of STP, E-STP, EHI, and E-EHI also showed notable distinctions between EC 711 and TC Yagi. Compared to individual parameters, composite parameters were much better collocated with high-tornado-density regions.

Similar to the skill of E-CAPE relative to MLCAPE, E-STP and E-EHI showed much better collocations with the high-tornado-density areas than STP and EHI (Fig. 14). The better performances of E-STP and E-EHI over STP and EHI were more apparent in the EC case than the TC case, possibly because the TC Yagi environment is moister and thus less impact from dry air entrainment. In addition, the better performance of E-STP over STP was more apparent than that of E-EHI over EHI. Over period A for EC 711, the maximum E-STP and E-EHI values appeared in western Shandong Province, superposing the tornadogenesis area, with values exceeding 5 and 4.5, respectively (Figs. 14d,j). Over period B for EC 711, the maximum E-STP and E-EHI values were slightly smaller than those in period A and shifted

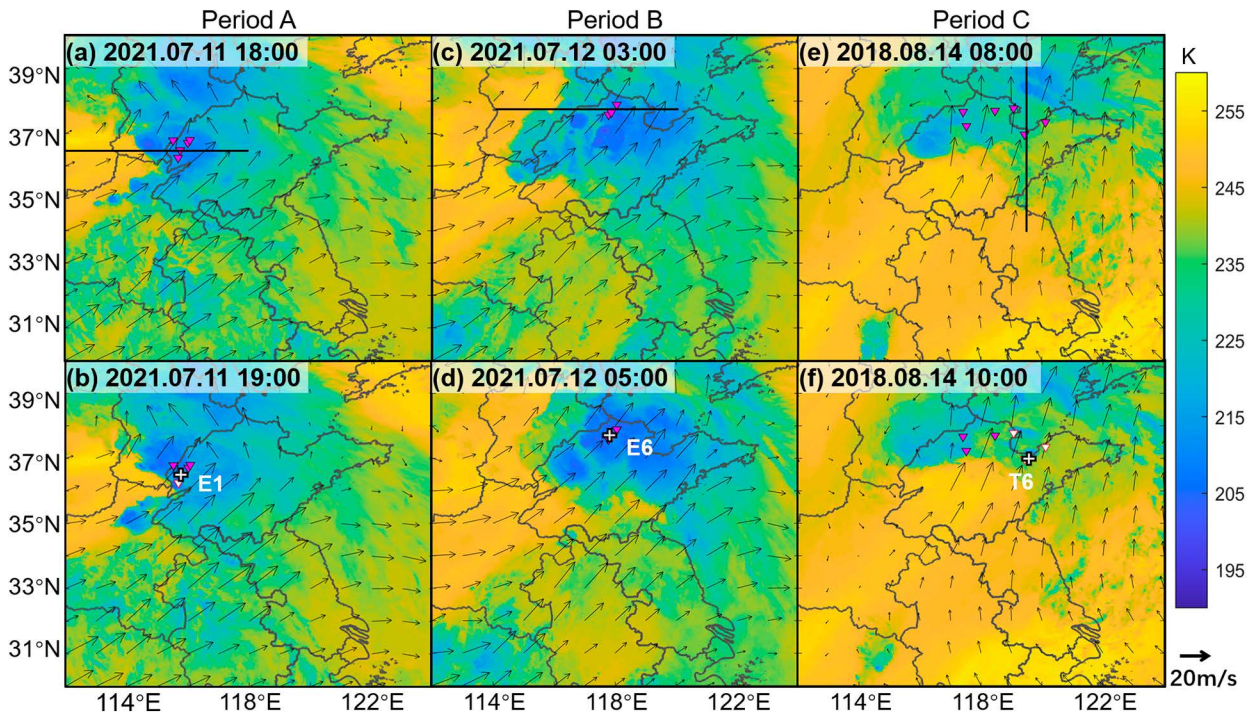


FIG. 16. Brightness temperature (shaded; K) in the channel-9 water vapor imagery of the *Himawari-8* satellite (near 400 hPa) and wind at 400 hPa (vectors; m s^{-1}) at (a) 1800 and (b) 1900 BJT 11 Jul 2021 for period A, (c) 0300 and (d) 0500 BJT 12 Jul 2021 for period B, and (e) 0800 and (f) 1000 BJT 14 Aug 2018 for period C. The triangles pointing down indicate the tornadoes occurring during each period with the white ones denoting the tornadoes occurring at the panel time. The black lines denote the positions of the cross sections in Fig. 17. The white crosses denote the positions of E1, E6, and T6 of the skew T diagrams plotted in Fig. 20.

slightly northward, consistent with the locations of tornado clusters (Figs. 14e,k).

The skill of E-EHI was not as good as E-STP in EC 711 case especially in period B, which can be clearly seen in the higher E-EHI than E-STP in the areas with no tornadogenesis in Fig. 14k relative to Fig. 14e, possibly because E-EHI only considers E-CAPE and SRH1 which both had a large magnitude in that area (Figs. 10h and 12e), while E-STP also includes the effect of SHR6 (Fig. 12b) and MLLCL [see Eq. (4)]. On the other hand, the high terrain in southern Shandong Province (shaded in Fig. 1b) may be a mitigating factor that prevents tornadogenesis despite large E-EHI and E-STP in that region.

For TC Yagi over period C, the region with the largest E-STP and E-EHI values existed only in northern Shandong Province, highly consistent with the positions where tornadoes occurred, but the E-STP and E-EHI values were approximately 3.5 and 2, respectively (Figs. 14f,l), much smaller than those of EC 711. As a result, EC 711, including period A and period B, offered an environment much more favorable for tornado development than TC Yagi.

4) COMPARISON WITH U.S. STATISTICS

The thermodynamic, kinematic, and composite parameters in these two tornado outbreak events were compared with those in the United States described in Edwards et al. (2012) (Fig. 15). No significant differences were found in STP of

these two events from non-TC and TC cases in the United States (Fig. 15d). Relative to TC cases in the United States, TC Yagi had a smaller SRH1 (Fig. 15b) likely due to its weaker intensity (the average intensity of U.S. tornadic TCs from 2007 to 2021 was 26 m s^{-1} at tornadogenesis times in terms of the surface maximum wind speed near TC centers, while the corresponding intensity of TC Yagi was 16 m s^{-1}), which was balanced by a larger MLCAPE (Fig. 15a) and 700–500-hPa lapse rate (Fig. 15c). Relative to non-TC cases in the United States, EC 711 had a similar SRH1 (Fig. 15b) but a smaller MLCAPE (Fig. 15a) and larger 700–500-hPa lapse rate (Fig. 15c).

c. Impact of moisture and the role of dry air intrusion

Considering that E-CAPEs were better collocated with tornado outbreak locations, and can be apparently affected by moisture, impact of dry air intrusion on the three periods were examined. We defined dry air in this work whenever the relative humidity is no larger than 50%. We chose three tornadoes whose E-CAPE evolutions were representative of the three periods, namely the first and sixth tornadoes for EC 711 and the sixth tornado for TC Yagi, which are denoted as E1, E6, and T6.

In the EC 711 case, moisture-channel satellite observation showed an apparent dry air intrusion from the west of the tornado outbreak region at ~ 400 hPa (Figs. 16a–d). ERA5 analysis showed that the upper-level dry air with relative humidity

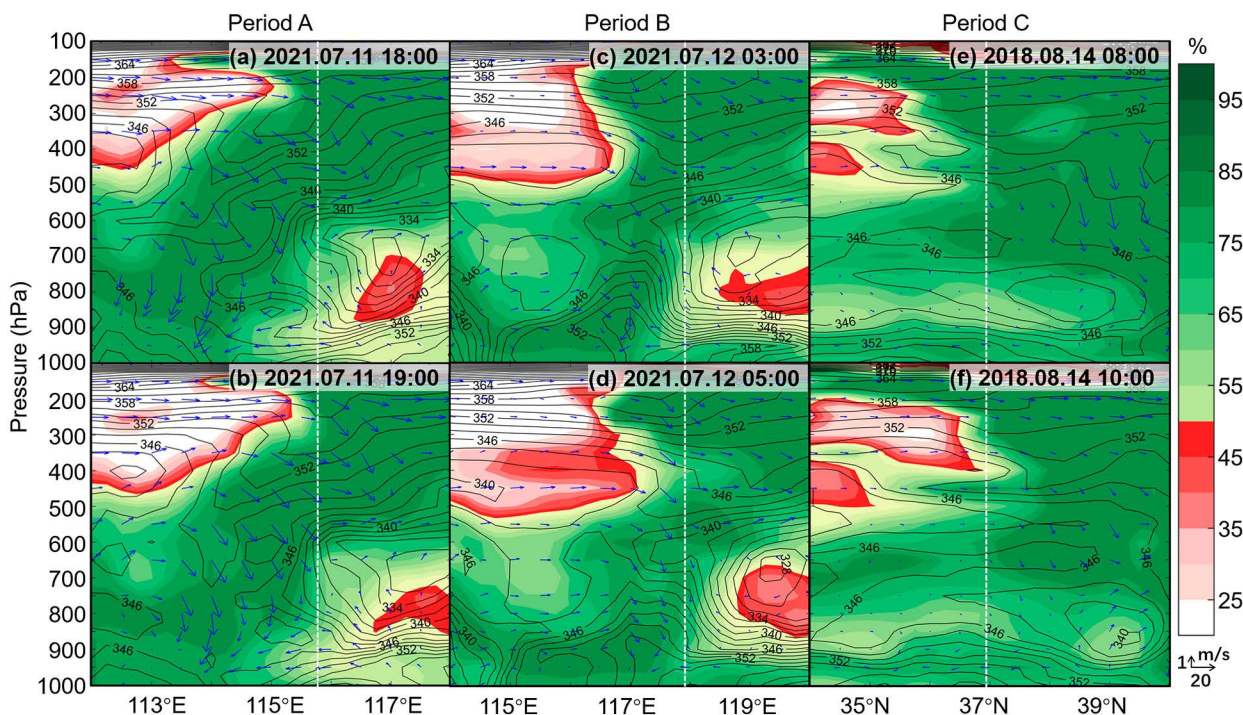


FIG. 17. Cross sections of relative humidity (shaded; %), equivalent potential temperature (black contours; K), and wind in the cross section (vectors; m s^{-1}) at (a) 1800 and (b) 1900 BJT 11 Jul 2021 for period A, (c) 0300 and (d) 0500 BJT 12 Jul 2021 for period B, and (e) 0800 and (f) 1000 BJT 14 Aug 2018 for period C. The white dotted lines denote the position of tornadoes E1, E6, and T6 occurring at the bottom panel time.

below 50% centered at ~ 300 hPa did not apparently intrude down to the boundary layer (Figs. 17a–d). A dry airstream was also observed in the lower troposphere centered at ~ 800 hPa (Figs. 17a–d) east and northeast of the tornado region propagating eastward under the background of southwesterly low-level jet (Figs. 18a–d). However, by examining the average hourly evolution of various parameters at the grid points that are closest to each tornado using sounding derived from ERA5 analyses (Figs. 19a–d), no apparent impact of these dry air features on tornado outbreak potential was found. During the 4 h before tornadogenesis, the midlevel relative humidity was increasing (up to above 80% at tornadogenesis time), and the lapse rate at middle and low levels slowly decreased rather than increased as generally speculated from evaporative cooling of stratus clouds in the ambient environment. Since this event occurred at night, there was no impact on lapse rate from insolation point of view either. The increase of E-CAPE within 1 h before tornadogenesis in period A and 5 h before tornadogenesis in period B was more consistent with the increasing moisture (Figs. 19a–d) advected by the low-level jet in the southeast quadrant of EC circulation (Figs. 18a–d). These features can be clearly seen also in the evolution of skew- T diagrams derived from ERA5 analyses at E1 and E6 (Figs. 20a,b).

In the TC Yagi case, moisture-channel satellite observation (Figs. 16e,f) and ERA5 analyses (Figs. 17e,f) also showed an apparent dry air intrusion from the south of the tornado outbreak region at ~ 400 hPa. The average relative humidity at tornadogenesis locations at 400 hPa decreased sharply within

2 h before tornadogenesis (Fig. 19e), from nearly saturated at 0800 BJT to quite dry at 1000 BJT (Fig. 20c). The low-level environment was generally moist without much change in relative humidity in the tornado region with an average of above 80%. In this case, upper-level dry air may have had positive impact in increasing the low-level lapse rate through increasing surface temperature with the intrusion of upper level dry air eroding cloudiness. From 0800 to 1000 BJT 14 August 2018, dry air at about 400 hPa intruded from south into the area where tornadoes formed (Figs. 16e,f). As the dry air intruded, the stratiform precipitation faded from south to north (Figs. 21a–c). The region of tornado outbreak received more solar heating with the erosion of cloudiness (Figs. 21d–f), causing surface temperature to rise (Figs. 21g–i, 20c, and 19f). As a result, the lapse rate from the surface to middle levels increased (Figs. 21j–l, 20c, and 19f), leading to an increase in E-CAPE (Figs. 20c and 19f), which is favorable for tornadogenesis. Similar to EC 711, we did not find an apparent increase in lapse rate due to the midlevel's evaporative cooling of stratus clouds in the ambient environment (Fig. 20c).

Our analyses on the impact of dry air suggest a big challenge in using infrequent and widely spaced conventional radiosonde observations even at a location quite close to tornadogenesis, in assessing the impact of dry air on tornado outbreak potential. Large temporal changes in E-CAPE, lapse rate, surface temperature, and relative humidity were found approaching to tornadogenesis hour by hour (Fig. 19). Favorable changes of E-CAPE and moisture occurred mainly 1–5 h

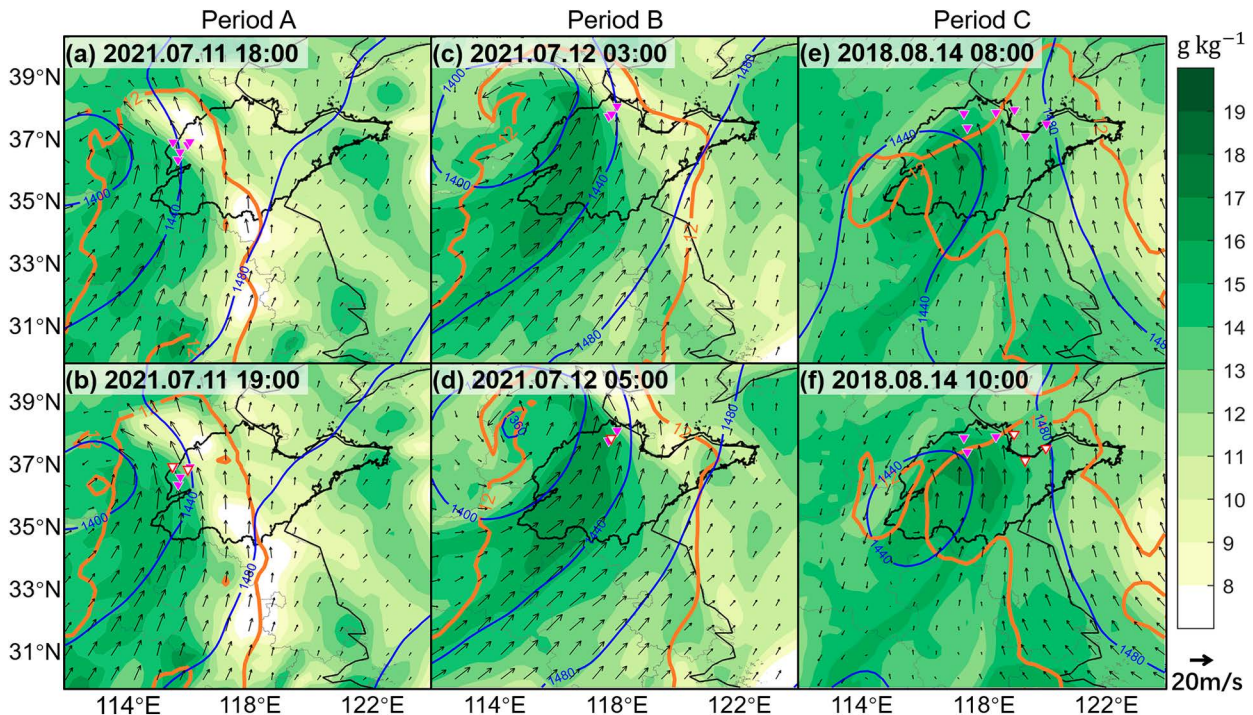


FIG. 18. Geopotential heights (blue contours; gpm), specific humidity (shaded; g kg^{-1}), wind (vectors; m s^{-1}), and the low-level jet denoted by the wind speed contour of 12 m s^{-1} at 850 hPa (orange) at (a) 1800 and (b) 1900 BJT 11 Jul 2021 for period A, (c) 0300 and (d) 0500 BJT 12 Jul 2021 for period B, and (e) 0800 and (f) 1000 BJT 14 Aug 2018 for period C. The triangles pointing down indicate the tornadoes occurring during each period with the white ones denoting the tornadoes occurring at the panel time.

before tornadogenesis at tornado locations, which suggests that using conventional radiosondes with a 12-h interval may not be able to capture important signals for tornadogenesis potential. In addition, considering the much smaller region of high E-CAPE relative to MLCAPE, and tornadoes usually occur in the overlapping area between E-CAPE and SRH1, using conventional radiosondes that are usually not quite close to the tornadogenesis location to assess tornado outbreak potential is very difficult. Curtis (2004) demonstrated that tornado outbreaks tended to occur in the strong gradient of midlevel relative humidity where parameters support the development of mesocyclones. A sounding that is located on the dry side of the strong gradient does not represent the environment of tornadogenesis on the wet side of the strong gradient. In other words, a proximity sounding, which was defined as within 3 h and 185 km from tornadogenesis by McCaul (1991), that shows apparent midlevel dry air intrusion does not necessarily guarantee an important impact from dry air intrusion on the tornadogenesis around it. The tornadogenesis could be just due to the increasing moisture on the wet side of the strong gradient zone of midlevel relative humidity. Whether dry air intrusion is just associated with tornado outbreaks or has an apparent contribution needs detailed diagnosis on high-resolution temporal and spatial radiosondes or numerical experiments.

6. Summary

This work examined features of the only two documented tornado outbreak events in China. One was EC 711, and the

other was TC Yagi; these events produced tornadoes mainly in Shandong Province in summer. The distinctions in the characteristics of the tornadoes and their parent storms as well as the environmental features between these two tornado outbreak events were explored.

EC 711 generated 13 tornadoes in total, most of which were located in the southeast quadrant of the EC, while TC Yagi produced 11 tornadoes in total, most of which occurred in the northeast quadrant of the TC. These two events occurred in an environment that was quite typically favorable for tornado outbreaks. EC 711 was associated with a strong midlevel jet between the westerly trough extending southwestward from the EC center and the subtropical high to the southeast, while TC Yagi was located south of a westerly trough, west of the subtropical high, and on the right entrance of a strong upper-level jet streak (200 hPa) located to the north. In both events, the southerly low-level jets advected abundant warm moist air to Shandong Province, and the southwesterly wind at 500 hPa over the southeasterly wind at the surface produced veering wind shear in the tornadogenesis regions, with that of EC 711 being stronger with more apparent veering pattern than that of TC Yagi.

The K index and E-CAPE had better collocation with the tornadogenesis region than MLCAPE, possibly due to their sensitivity to midlevel moisture. A better collocation among E-CAPE, SHR6 and SRH1 was found in TC Yagi than in EC 711. E-CAPE was better collocated with tornadogenesis region than dynamic parameters such as SHR6 and SRH1 in

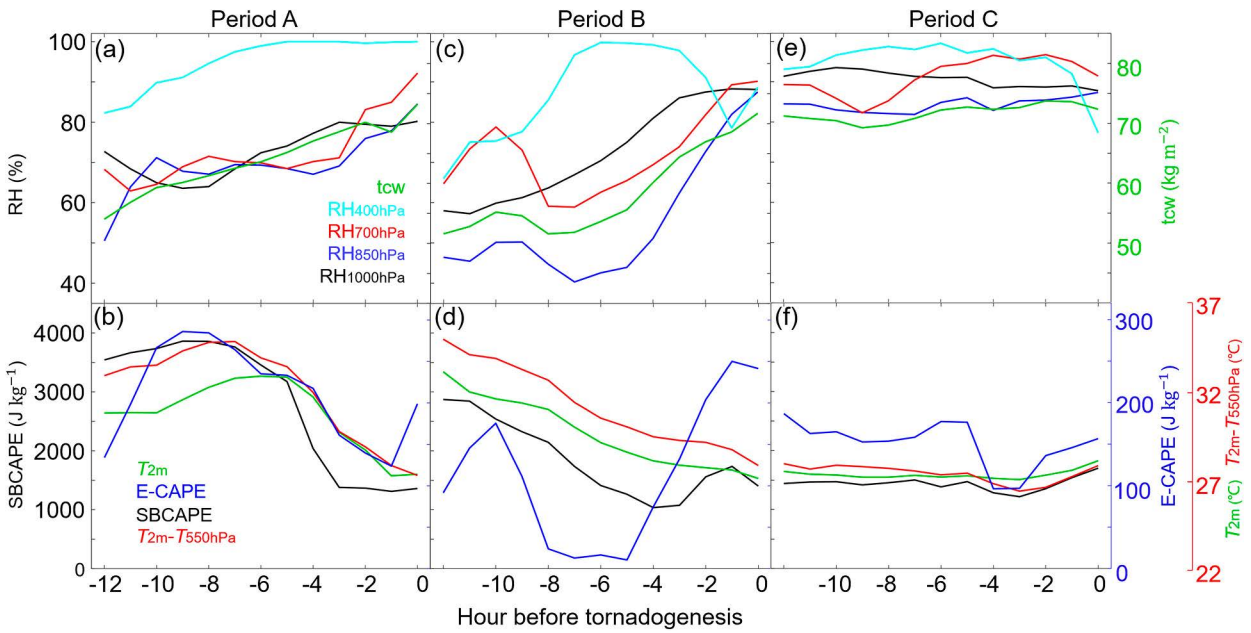


FIG. 19. Hourly variations of (a),(c),(e) relative humidity (RH) at 400, 700, 850, and 1000 hPa, and total column water (tcw; kg m⁻²); (b),(d),(f) surface-based CAPE (SBCAPE), E-CAPE, temperature at 2 m above ground level (AGL), and temperature difference between 2 m AGL and 550 hPa averaged over all tornadoes in each period. The “0” on the x axis represents the time of tornadogenesis, while negative numbers on the x axis indicate hours before tornadogenesis.

EC 711. Among all parameters, the composite parameter E-STP was collocated the best with the tornadogenesis region for both events, with that of EC 711 being larger than that of TC Yagi. In addition, no significant differences were found in

STP of these two events from their counterparts in the United States. TC Yagi had a smaller SRH1, likely due to its weaker intensity compared to TCs in the United States, but a larger instability than TC tornado outbreak events in the United

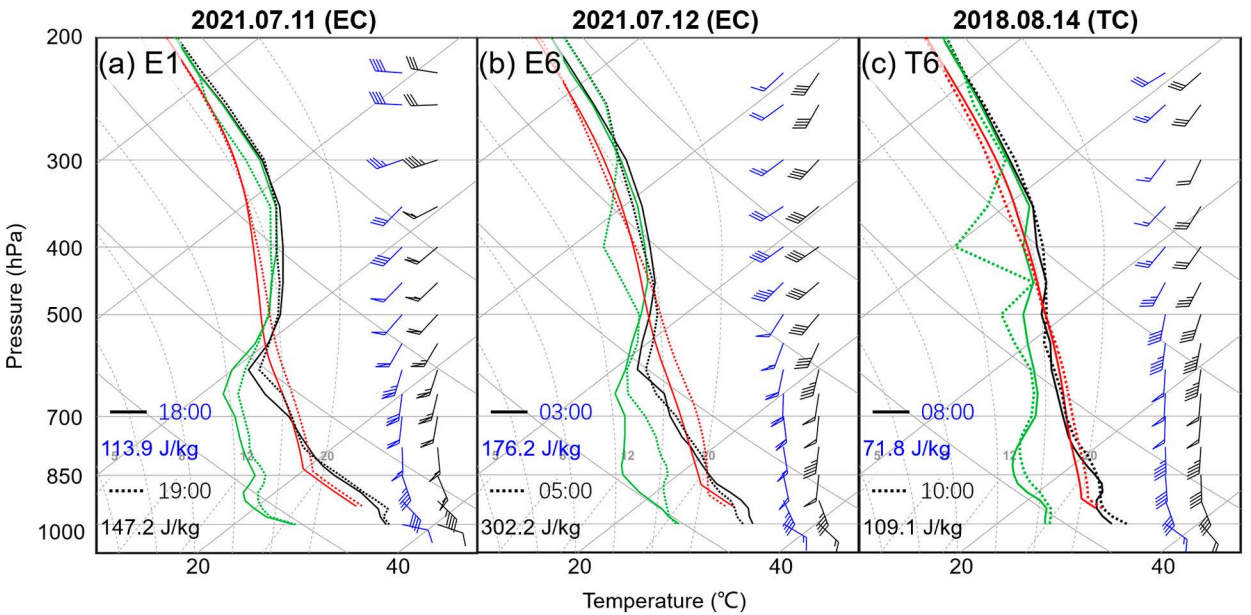


FIG. 20. (a) Skew *T* diagrams at the cross marks (a) E1 at 1800 (solid with blue wind barbs) and 1900 BJT (dotted with black wind barbs) 11 Jul 2021. The red lines denote the lapse rate for a mixed-layer parcel considering entrainment. (b),(c) As in (a), but for E6 at 0300 and 0500 BJT 12 Jul 2012, and T6 at 0800 and 1000 BJT 14 Aug 2018, respectively. The locations of E1, E6, and T6 are given in Figs. 16b, 16d, and 16f. Half barbs, full barbs, and pennants represent 2, 4, and 20 m s⁻¹, respectively. The values in the bottom-left corner of each panel indicate the E-CAPE.

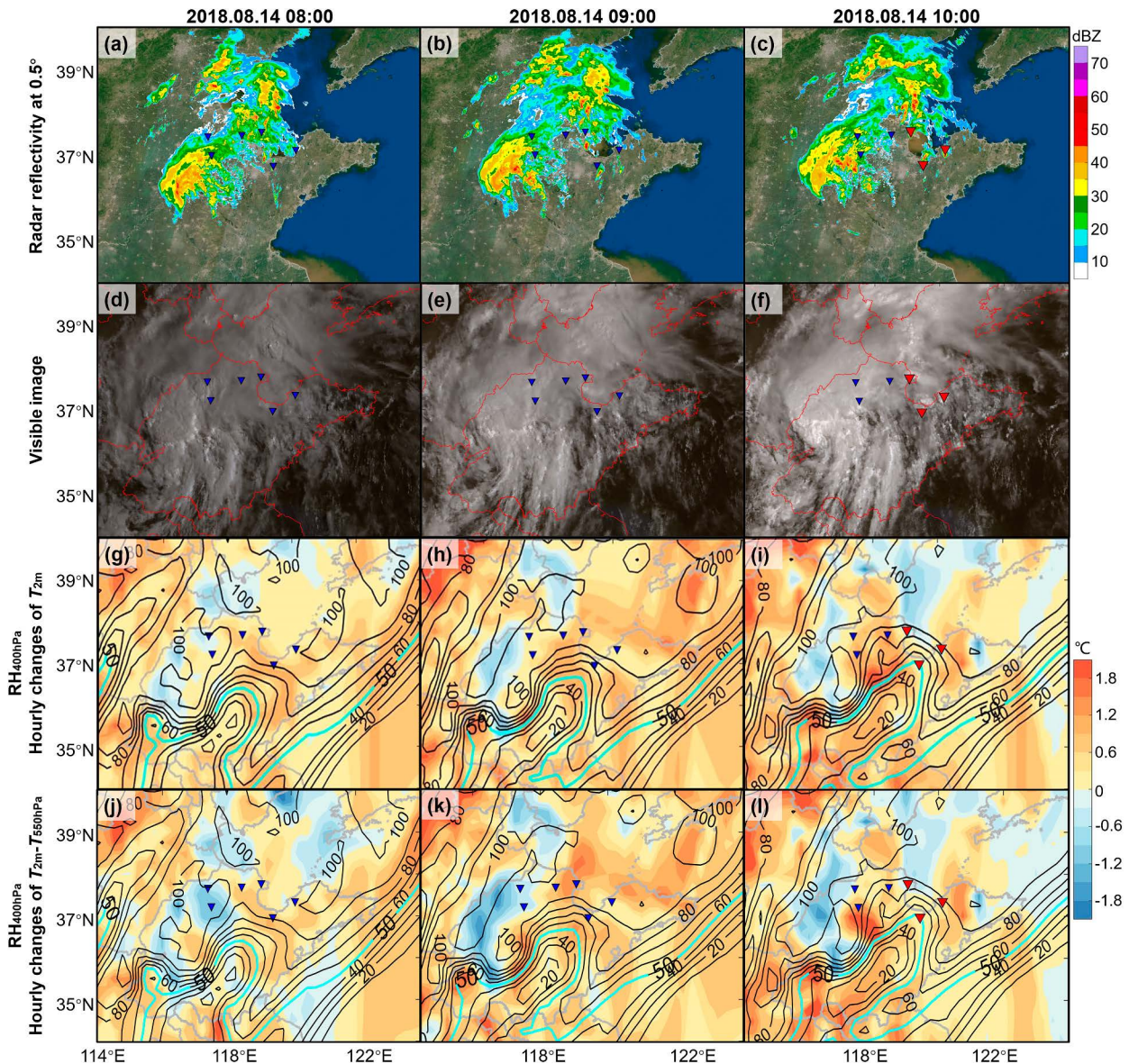


FIG. 21. (a)–(c) Radar base reflectivity (dBZ) at 0.5° elevation at Binzhou, (d)–(f) visible images of the *Himawari-8* satellite, (g)–(i) relative humidity at 400 hPa (contours with an interval of 10%) and change of T_{2m} at the panel time from the previous hour (shaded; $^\circ\text{C}$), and (j)–(l) relative humidity at 400 hPa (contours with an interval of 10%) and change of $T_{2m} - T_{500\text{hPa}}$ (shaded; $^\circ\text{C}$) at the panel time from the previous hour, at (left) 0800, (center) 0900, and (right) 1000 BJT 14 Aug 2018. The triangles pointing down indicate the tornadoes occurring during each period with the red ones denoting the tornadoes occurring at the panel time.

States, while EC 711 had a similar SRH1 but a slightly smaller instability than non-TC tornado outbreak events in the United States.

The distinctions in the convective parameters between the two events may have been due to the strength and structure of the cyclones. First, EC 711 had lower MSLPs over both periods than TC Yagi, suggesting relatively strong synoptic forcing and thus a better convective environment in EC 711. These differences may have caused the larger lapse rate and thus larger instability as well as the higher southwesterly wind speed at 500 hPa in EC 711. Second, although both events had

similar near-surface winds, different baroclinicity of the cyclones caused different juxtapositions between the tornado outbreak region and the cyclone center, resulting in more apparent veering wind shear and larger magnitudes in SHR6 and SRH1 in the EC 711 case than in the TC case. The larger differences in the wind profile in vertical in the EC event is possibly the reason for its poorer collocation between E-CAPE and SHR6.

Results on the impact of dry air on tornadogenesis using hourly ERA5 analyses at tornado locations provided new insight on the scale of dry air impact on tornadogenesis potential,

relative to previous speculations obtained mainly using radiosondes with coarse temporal and spatial resolutions. Even though apparent dry air was observed at the upper troposphere from the west and also at the midtroposphere on the east of tornadogenesis area in EC 711, no apparent impact from dry air intrusion was found on the increase of E-CAPE leading up to tornadogenesis. The increased E-CAPE seemed to have resulted from enhanced moisture transported by a southwesterly low-level jet southeast of the EC center. However, in the TC Yagi case, dry air at the upper levels from the south may have helped to heat the surface through erosion of cloudiness and thus increased the mid- to low-level lapse rates and E-CAPE, rather than through evaporative cooling of stratus clouds in the ambient environment at middle levels. Large hourly variation of various parameters suggests that using a conventional radiosonde not close to tornado locations at a 12-h interval may not be able to accurately predict the potential of tornadogenesis or tornado outbreak.

Apparent differences were found in the dominant mode, strength, diameter, and duration of the parent storms of the tornadoes between the two events. Most of the parent storms of tornadoes associated with EC 711 were supercells embedded in the QLCS and cluster, whereas most of the parent storms of tornadoes related to TC Yagi were discrete cellular minisupercells. The tornadic mesocyclones in EC 711 were stronger, larger and more long-lived than those in TC Yagi; The TVSS in EC 711 were also stronger than those in TC Yagi, which was possibly due to the higher instability and vertical wind shear and thus higher E-STP of EC 711 than those of TC Yagi.

Acknowledgments. This work was sponsored by the National Natural Science Foundation of China (Grants 42030604 and 41875051).

Data availability statement. Radar data were provided by the National Meteorological Information Center of the China Meteorological Administration (available online at <https://data.cma.cn/data/cdcindex/cid/0b9164954813c573.html>). The ERA5 reanalysis data were downloaded from <https://cds.climate.copernicus.eu/cdsapp#!/dataset/reanalysis-era5-single-levels?tab=overview> and <https://cds.climate.copernicus.eu/cdsapp#!/dataset/reanalysis-era5-pressure-levels?tab=overview>. The brightness temperature data in water vapor channel 9 of the *Himawari-8* satellite were downloaded from <https://www.eorc.jaxa.jp/ptree/index.html>.

REFERENCES

- Anderson-Frey, A. K., Y. P. Richardson, A. R. Dean, R. L. Thompson, and B. T. Smith, 2018: Near-storm environments of outbreak and isolated tornadoes. *Wea. Forecasting*, **33**, 1397–1412, <https://doi.org/10.1175/WAF-D-18-0057.1>.
- Bai, L., 2021: Environmental analysis on the first documented tornado outbreak in China. *Atmos. Sci. Lett.*, **22**, e1057, <https://doi.org/10.1002/asl.1057>.
- , G. Chen, and L. Huang, 2020a: Image processing of radar mosaics for the climatology of convection initiation in South China. *J. Appl. Meteor. Climatol.*, **59**, 65–81, <https://doi.org/10.1175/JAMC-D-19-0081.1>.
- , Z. Meng, K. Sueki, G. Chen, and R. Zhou, 2020b: Climatology of tropical cyclone tornadoes in China from 2006 to 2018. *Sci. China Earth Sci.*, **63**, 37–51, <https://doi.org/10.1007/s11430-019-9391-1>.
- , —, R. Zhou, G. Chen, N. Wu, and W.-K. Wong, 2022: Radar-based characteristics and formation environment of supercells in the landfalling Typhoon Mujigae in 2015. *Adv. Atmos. Sci.*, **39**, 802–818, <https://doi.org/10.1007/s00376-021-1013-2>.
- Baker, A. K., M. D. Parker, and M. D. Eastin, 2009: Environmental ingredients for supercells and tornadoes within Hurricane Ivan. *Wea. Forecasting*, **24**, 223–244, <https://doi.org/10.1175/2008WAF2222146.1>.
- Bunkers, M. J., B. A. Klimowski, J. W. Zeitler, R. L. Thompson, and M. L. Weisman, 2000: Predicting supercell motion using a new hodograph technique. *Wea. Forecasting*, **15**, 61–79, [https://doi.org/10.1175/1520-0434\(2000\)015<0061:Psmuan>2.0.CO;2](https://doi.org/10.1175/1520-0434(2000)015<0061:Psmuan>2.0.CO;2).
- Cohen, A. E., 2010: Synoptic-scale analysis of tornado-producing tropical cyclones along the Gulf Coast. *Natl. Wea. Dig.*, **34**, 99–115.
- Curtis, L., 2004: Midlevel dry intrusions as a factor in tornado outbreaks associated with landfalling tropical cyclones from the Atlantic and Gulf of Mexico. *Wea. Forecasting*, **19**, 411–427, [https://doi.org/10.1175/1520-0434\(2004\)019<0411:MDIAAF>2.0.CO;2](https://doi.org/10.1175/1520-0434(2004)019<0411:MDIAAF>2.0.CO;2).
- Davies-Jones, R. P., 1984: Streamwise vorticity: The origin of updraft rotation in supercell storms. *J. Atmos. Sci.*, **41**, 2991–3006, [https://doi.org/10.1175/1520-0469\(1984\)041<2991:SVTOOU>2.0.CO;2](https://doi.org/10.1175/1520-0469(1984)041<2991:SVTOOU>2.0.CO;2).
- , D. W. Burgess, and M. P. Foster, 1990: Test of helicity as a tornado forecast parameter. Preprints, *16th Conf. on Severe Local Storms*, Kananaskis Park, Alberta, Canada, Amer. Meteor. Soc., 588–592.
- Edwards, R., A. R. Dean, R. L. Thompson, and B. T. Smith, 2012: Convective modes for significant severe thunderstorms in the contiguous United States. Part III: Tropical cyclone tornadoes. *Wea. Forecasting*, **27**, 1507–1519, <https://doi.org/10.1175/WAF-D-11-00117.1>.
- Fulton, R. A., J. P. Breidenbach, D.-J. Seo, D. A. Miller, and T. O'Bannon, 1998: The WSR-88D rainfall algorithm. *Wea. Forecasting*, **13**, 377–395, [https://doi.org/10.1175/1520-0434\(1998\)013<0377:TWRA>2.0.CO;2](https://doi.org/10.1175/1520-0434(1998)013<0377:TWRA>2.0.CO;2).
- Galway, J. G., 1977: Some climatological aspects of tornado outbreaks. *Mon. Wea. Rev.*, **105**, 477–484, [https://doi.org/10.1175/1520-0493\(1977\)105<0477:SCAOTO>2.0.CO;2](https://doi.org/10.1175/1520-0493(1977)105<0477:SCAOTO>2.0.CO;2).
- Gentry, R. C., 1983: Genesis of tornadoes associated with hurricanes. *Mon. Wea. Rev.*, **111**, 1793–1805, [https://doi.org/10.1175/1520-0493\(1983\)111<1793:GOTAWH>2.0.CO;2](https://doi.org/10.1175/1520-0493(1983)111<1793:GOTAWH>2.0.CO;2).
- Hamill, T. M., R. S. Schneider, H. E. Brooks, G. S. Forbes, H. B. Bluestein, M. Steinberg, D. Melendez, and R. M. Dole, 2005: The May 2003 extended tornado outbreak. *Bull. Amer. Meteor. Soc.*, **86**, 531–542, <https://doi.org/10.1175/BAMS-86-4-531>.
- Johns, R. H., and C. A. Doswell III, 1992: Severe local storms forecasting. *Wea. Forecasting*, **7**, 588–612, [https://doi.org/10.1175/1520-0434\(1992\)007<0588:SLSF>2.0.CO;2](https://doi.org/10.1175/1520-0434(1992)007<0588:SLSF>2.0.CO;2).
- Lu, X., H. Yu, M. Ying, B. Zhao, S. Zhang, L. Lin, L. Bai, and R. Wan, 2021: Western North Pacific tropical cyclone database created by the China Meteorological Administration. *Adv. Atmos. Sci.*, **38**, 690–699, <https://doi.org/10.1007/s00376-020-0211-7>.
- Markowski, P., and Y. Richardson, 2010: *Mesoscale Meteorology in Midlatitudes*. Wiley-Blackwell, 430 pp.

- McCaul, E. W., Jr., 1987: Observations of the hurricane “Danny” tornado outbreak of 16 August 1985. *Mon. Wea. Rev.*, **115**, 1206–1223, [https://doi.org/10.1175/1520-0493\(1987\)115<1206:OOTHTO>2.0.CO;2](https://doi.org/10.1175/1520-0493(1987)115<1206:OOTHTO>2.0.CO;2).
- , 1991: Buoyancy and shear characteristics of hurricane-tornado environments. *Mon. Wea. Rev.*, **119**, 1954–1978, [https://doi.org/10.1175/1520-0493\(1991\)119<1954:BASCOH>2.0.CO;2](https://doi.org/10.1175/1520-0493(1991)119<1954:BASCOH>2.0.CO;2).
- , 1993: Observations and simulations of hurricane-spawned tornadic storms. *The Tornado: Its Structure, Dynamics, Prediction and Hazards, Geophys. Monogr.*, Vol. 79, Amer. Geophys. Union, 120–142, <https://doi.org/10.1029/GM079p0119>.
- , D. E. Buechler, S. J. Goodman, and M. Cammarata, 2004: Doppler radar and lightning network observations of a severe outbreak of tropical cyclone tornadoes. *Mon. Wea. Rev.*, **132**, 1747–1763, [https://doi.org/10.1175/1520-0493\(2004\)132<1747:DRALNO>2.0.CO;2](https://doi.org/10.1175/1520-0493(2004)132<1747:DRALNO>2.0.CO;2).
- Meng, Z., and D. Yao, 2014: Damage survey, radar, and environment analyses on the first-ever documented tornado in Beijing during the heavy rainfall event of 21 July 2012. *Wea. Forecasting*, **29**, 702–724, <https://doi.org/10.1175/WAF-D-13-00052.1>.
- Mercer, A. E., C. M. Shafer, C. A. Doswell III, L. M. Leslie, and M. B. Richman, 2012: Synoptic composites of tornadic and nontornadic outbreaks. *Mon. Wea. Rev.*, **140**, 2590–2608, <https://doi.org/10.1175/MWR-D-12-00029.1>.
- Molinari, J., D. M. Romps, D. Vollaro, and L. Nguyen, 2012: CAPE in tropical cyclones. *J. Atmos. Sci.*, **69**, 2452–2463, <https://doi.org/10.1175/JAS-D-11-0254.1>.
- Moore, T. W., and R. W. Dixon, 2011: Climatology of tornadoes associated with Gulf Coast-landfalling hurricanes. *Geogr. Rev.*, **101**, 371–395, <https://doi.org/10.1111/j.1931-0846.2011.00102.x>.
- , and —, 2015: Patterns in 500 hPa geopotential height associated with temporal clusters of tropical cyclone tornadoes. *Meteor. Appl.*, **22**, 314–322, <https://doi.org/10.1002/met.1456>.
- Newton, C. W., 1967: Severe convective storms. *Adv. Geophys.*, **12**, 257–308, [https://doi.org/10.1016/S0065-2687\(08\)60377-5](https://doi.org/10.1016/S0065-2687(08)60377-5).
- Novlan, D. J., and W. M. Gray, 1974: Hurricane-spawned tornadoes. *Mon. Wea. Rev.*, **102**, 476–488, [https://doi.org/10.1175/1520-0493\(1974\)102<0476:HST>2.0.CO;2](https://doi.org/10.1175/1520-0493(1974)102<0476:HST>2.0.CO;2).
- Rasmussen, E. N., and D. O. Blanchard, 1998: A baseline climatology of sounding-derived supercell and tornado forecast parameters. *Wea. Forecasting*, **13**, 1148–1164, [https://doi.org/10.1175/1520-0434\(1998\)013<1148:ABCOSD>2.0.CO;2](https://doi.org/10.1175/1520-0434(1998)013<1148:ABCOSD>2.0.CO;2).
- Raveh-Rubin, S., 2017: Dry intrusions: Lagrangian climatology and dynamical impact on the planetary boundary layer. *J. Climate*, **30**, 6661–6682, <https://doi.org/10.1175/JCLI-D-16-0782.1>.
- Romps, D. M., and Z. Kuang, 2010: Do undiluted convective plumes exist in the upper tropical troposphere? *J. Atmos. Sci.*, **67**, 468–484, <https://doi.org/10.1175/2009JAS184.1>.
- Schenkel, B. A., M. Coniglio, and R. Edwards, 2021: How does the relationship between ambient deep-tropospheric vertical wind shear and tropical cyclone tornadoes change between coastal and inland environments? *Wea. Forecasting*, **36**, 539–566, <https://doi.org/10.1175/WAF-D-20-0127.1>.
- Shafer, C. M., A. E. Mercer, C. A. Doswell III, M. B. Richman, and L. M. Leslie, 2009: Evaluation of WRF forecasts of tornadic and nontornadic outbreaks when initialized with synoptic scale input. *Mon. Wea. Rev.*, **137**, 1250–1271, <https://doi.org/10.1175/2008MWR2597.1>.
- Sueki, K., and H. Niino, 2016: Toward better assessment of tornado potential in typhoons: Significance of considering entrainment effects for CAPE. *Geophys. Res. Lett.*, **43**, 12 597–12 604, <https://doi.org/10.1002/2016GL070349>.
- Thompson, R. L., R. Edwards, J. A. Hart, K. L. Elmore, and P. Markowski, 2003: Close proximity soundings within supercell environments obtained from the Rapid Update Cycle. *Wea. Forecasting*, **18**, 1243–1261, [https://doi.org/10.1175/1520-0434\(2003\)018<1243:CPSWSE>2.0.CO;2](https://doi.org/10.1175/1520-0434(2003)018<1243:CPSWSE>2.0.CO;2).
- , B. T. Smith, J. S. Grams, A. R. Dean, and C. Broyles, 2012: Convective modes for significant severe thunderstorms in the contiguous United States. Part II: Supercell and QLCS tornado environments. *Wea. Forecasting*, **27**, 1136–1154, <https://doi.org/10.1175/WAF-D-11-00116.1>.
- Tochimoto, E., and H. Niino, 2016: Structural and environmental characteristics of extratropical cyclones that cause tornado outbreaks in the warm sector: A composite study. *Mon. Wea. Rev.*, **144**, 945–969, <https://doi.org/10.1175/MWR-D-15-0015.1>.
- , K. Sueki, and H. Niino, 2019: Entraining CAPE for better assessment of tornado outbreak potential in the warm sector of extratropical cyclones. *Mon. Wea. Rev.*, **147**, 913–930, <https://doi.org/10.1175/MWR-D-18-0137.1>.
- Verbout, S. M., D. M. Schulz, L. M. Leslie, H. E. Brooks, D. J. Karoly, and K. L. Elmore, 2007: Tornado outbreaks associated with landfalling hurricanes in the North Atlantic basin: 1954–2004. *Meteor. Atmos. Phys.*, **97**, 255–271, <https://doi.org/10.1007/s00703-006-0256-x>.
- Ying, M., W. Zhang, H. Yu, X. Lu, J. Feng, Y. Fan, Y. Zhu, and D. Chen, 2014: An overview of the China Meteorological Administration tropical cyclone database. *J. Atmos. Oceanic Technol.*, **31**, 287–301, <https://doi.org/10.1175/JTECH-D-12-00119.1>.
- Zhou, R., Z. Meng, and L. Bai, 2022: Differences in tornado activities and key tornadic environments between China and the United States. *Int. J. Climatol.*, **42**, 367–384, <https://doi.org/10.1002/joc.7248>.